Cell Reports

Article

Potentiation of cholinergic and corticofugal inputs to the lateral amygdala in threat learning

Graphical abstract

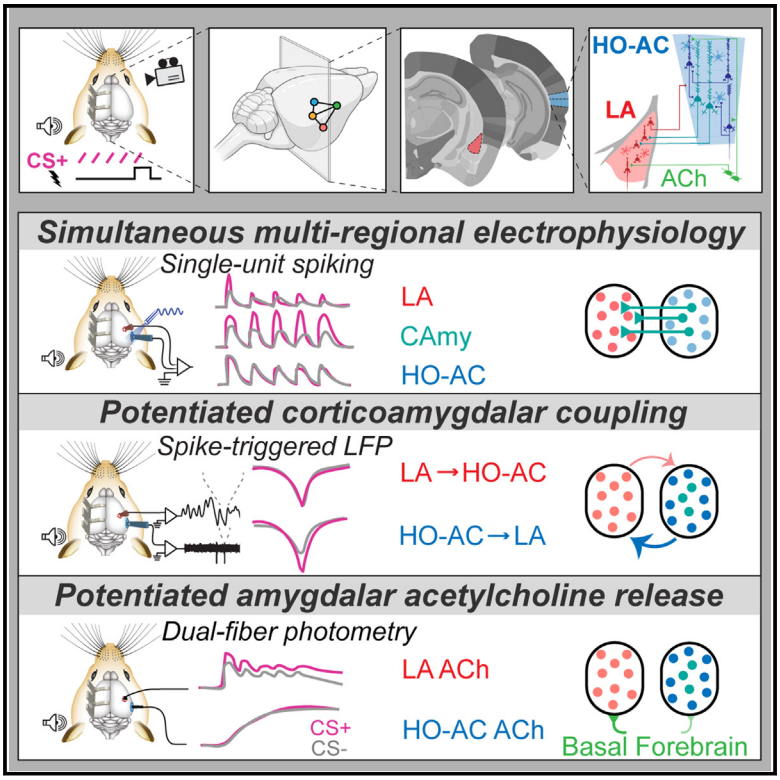

Highlights

- Pupil dilations and facial motions index auditory threat memory in head-fixed mice
- Multi-regional recordings of single units and acetylcholine in amygdala and cortex
- Associative plasticity in lateral amygdala and photo-tagged corticoamygdalar units
- Potentiated corticofugal and cholinergic inputs to amygdala during threat recall

Authors

Meenakshi M. Asokan, Yurika Watanabe, Eyal Y. Kimchi, Daniel B. Polley

Correspondence

ma0716@princeton.edu

In brief

Asokan et al. describe coordinated plasticity in a distributed network of brain regions during discriminative auditory threat learning. Corticofugal and cholinergic inputs to the lateral amygdala were potentiated during threat memory acquisition, consolidation, and recall, emphasizing discriminative plasticity in upstream inputs to the lateral amygdala that predicted threat memory strength.

Asokan et al., 2023, Cell Reports *42*, 113167
October 31, 2023
https://doi.org/10.1016/j.celrep.2023.113167

CellPress

Cell Reports

CellPress
OPEN ACCESS

Article

Potentiation of cholinergic and corticofugal inputs to the lateral amygdala in threat learning

Meenakshi M. Asokan,[1,2,5,7,*] Yurika Watanabe,[1] Eyal Y. Kimchi,[1,4,6] and Daniel B. Polley[1,2,3]
[1]Eaton-Peabody Laboratories, Massachusetts Eye and Ear, Boston, MA 02114, USA
[2]Division of Medical Sciences, Harvard Medical School, Boston, MA 02114, USA
[3]Department of Otolaryngology – Head and Neck Surgery, Harvard Medical School, Boston, MA 02114, USA
[4]Department of Neurology, Massachusetts General Hospital, Boston, MA 02114, USA
[5]Present address: Princeton Neuroscience Institute, Princeton, NJ 08540, USA
[6]Present address: Department of Neurology, Northwestern University, Chicago, IL 60208, USA
[7]Lead contact
*Correspondence: ma0716@princeton.edu
https://doi.org/10.1016/j.celrep.2023.113167

SUMMARY

The amygdala, cholinergic basal forebrain, and higher-order auditory cortex (HO-AC) regulate brain-wide plasticity underlying auditory threat learning. Here, we perform multi-regional extracellular recordings and optical measurements of acetylcholine (ACh) release to characterize the development of discriminative plasticity within and between these brain regions as mice acquire and recall auditory threat memories. Spiking responses are potentiated for sounds paired with shock (CS+) in the lateral amygdala (LA) and optogenetically identified corticoamygdalar projection neurons, although not in neighboring HO-AC units. Spike- or optogenetically triggered local field potentials reveal enhanced corticofugal—but not corticopetal—functional coupling between HO-AC and LA during threat memory recall that is correlated with pupil-indexed memory strength. We also note robust sound-evoked ACh release that rapidly potentiates for the CS+ in LA but habituates across sessions in HO-AC. These findings highlight a distributed and cooperative plasticity in LA inputs as mice learn to reappraise neutral stimuli as possible threats.

INTRODUCTION

Thriving, if not merely surviving, requires a well-calibrated risk management system to evaluate potential threats in the environment and deploy adaptive behavioral responses. Threat evaluation has been modeled with a Pavlovian auditory fear conditioning paradigm in which a neutral sound is subsequently paired with an aversive stimulus, producing defensive behaviors (e.g., freezing) and heightened autonomic responses (e.g., pupil dilation) elicited by the auditory conditioned stimulus (CS). Associative memory of the threatening sound is encoded by enhanced CS processing, synaptic plasticity, and genetic modifications in a distributed network of brain regions, although the amygdala complex is widely understood to be an essential hub in this network.[1–5]

Auditory CS inputs reach the amygdala via corticofugal and thalamic projections to the lateral amygdala (LA).[6–9] The amygdala—particularly the basolateral nucleus, but to a lesser extent the LA as well—is also innervated by basal forebrain cholinergic neurons.[10–12] Some cholinergic neurons in posterior basal forebrain regions exhibit vigorous short-latency phasic responses to a broad class of auditory stimuli,[13–17] suggesting three sources of auditory input to the amygdala—corticofugal, thalamic, and cholinergic—that could themselves be sites of plasticity upstream of the amygdala in auditory fear learning. Although associative auditory plasticity has been described in the thalamic,[18–20] cortical,[9,21] and cholinergic[22,23] inputs to the amygdala, these regions also receive feedback projections from the amygdala,[24–28] thereby making the primary development and directional flow of associative CS plasticity in these regions uncertain, at least when simple auditory stimuli are used as a CS (e.g., a tone burst).

Discriminative threat conditioning (DTC) can be distinguished from the broader class of Pavlovian auditory fear conditioning protocols by the use of a repeating sequence of relatively complex frequency-modulated (FM) sounds that either always (CS+) or never (CS−) predict the delayed onset of the aversive primary reinforcer.[29] Whereas auditory fear learning with simple sounds does not require the neocortex, associative threat memories acquired through DTC depend upon higher-order fields of the auditory cortex (HO-AC) and, even more specifically, their descending projection to the LA.[9,30] The nature or form of plasticity within the HO-AC and LA underlying the acquisition and recall of auditory threat memories can reflect dynamics in the functional coupling between brain regions,[31–33] as well as modifications in local circuit components within the neocortex,[9,29,34,35] as well as specific glutamatergic,[20] GABAergic,[36] and cholinergic[14] input pathways to the auditory cortex. Understanding the associative plasticity underlying DTC will benefit from approaches that pull the lens back to study coordinated changes between simultaneously recorded brain regions while also zooming in to

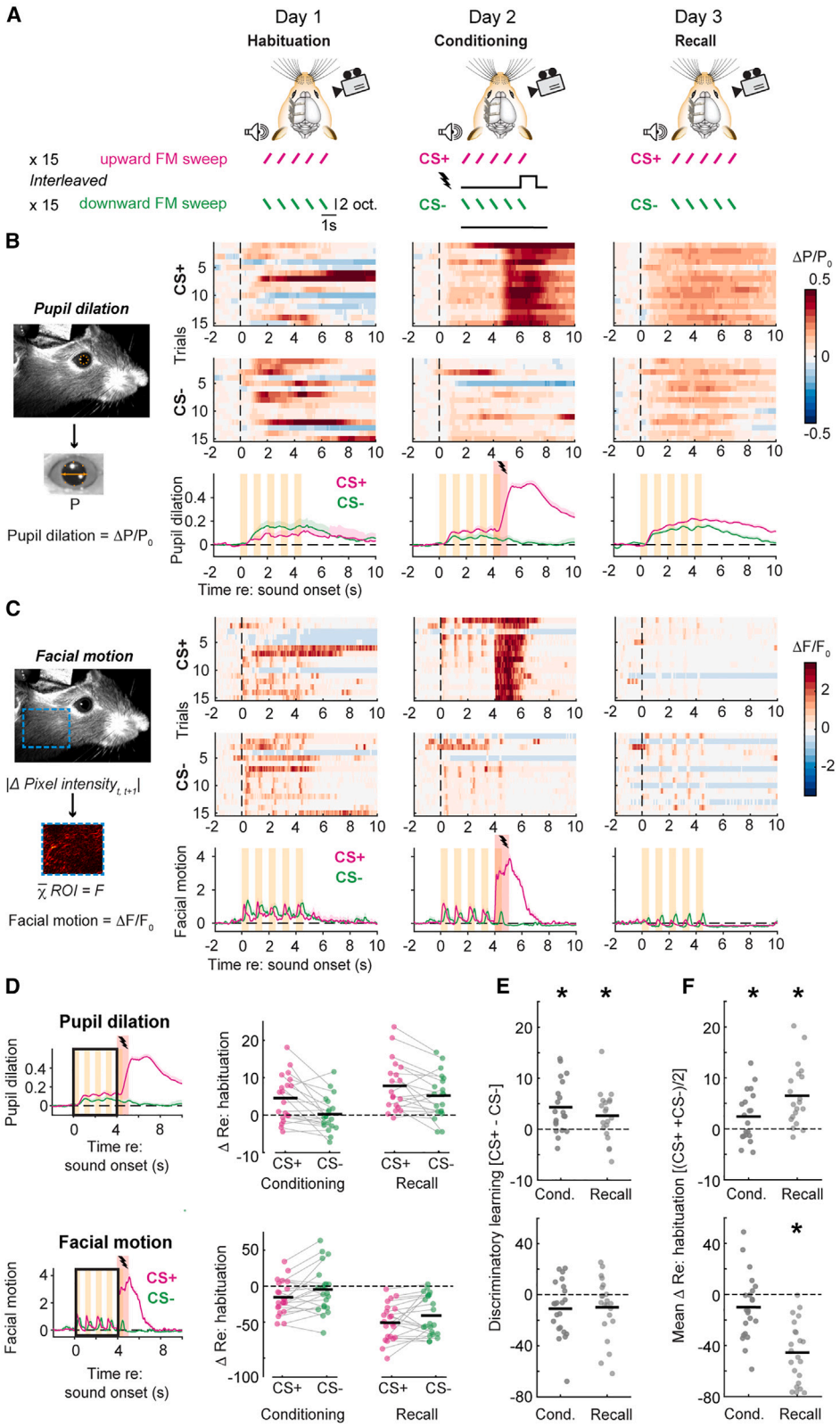

(legend on next page)

pinpoint changes in particular cell types that support reorganization across distributed brain networks. Here, we performed multi-regional measurements from key cell types in awake, head-fixed mice and identified relationships between associative plasticity and autonomic signatures of threat memory strength.

RESULTS

Sound-elicited facial movements and pupil dilation index discriminative threat conditioning in head-fixed mice

Behavioral evidence of DTC in rodents is typically indexed via whole-body movements such as escape or freezing. Autonomic markers also provide a rapid and sensitive measure of DTC, with the additional advantage of lending themselves to head-fixed neural recording preparations.[37] Here, we performed Pavlovian auditory delay conditioning in head-fixed mice over 3 consecutive days alongside quantitative videographic measurements of the face and pupil. The first (habituation) and third (recall) sessions presented interleaved trials of five upward and downward FM sweeps (Figure 1A). On day 2 of DTC (conditioning), a mild tail shock was initiated at the onset of the fifth FM sweep. The FM sweep direction paired with tail shock (i.e., the CS+) was counterbalanced across mice. In a separate cohort of pseudo-conditioned mice, an equivalent number of tail shocks was presented during the intertrial interval and was therefore not predictably related to either the upward or the downward FM CS.

Isoluminous pupil dilations were elicited by the novel FM sweep stimuli during the habituation session (Figure 1B, left) and also by tail shock in the conditioning session (Figure 1B, center). Pupil dilation also indexed discriminative learning, as evidenced by increased dilation beginning at the onset of the CS+ during the conditioning and recall sessions (Figure 1B, right).[34,38,39] We also noted that FM sweeps elicited rapid facial twitches that could be documented by measuring the motion energy within a region of interest positioned caudal to the vibrissa array (Figure 1C).[40–42] Like isoluminous pupil dilation, facial motion was elicited by sound and by tail shock and exhibited associative changes in response amplitude at the onset of the CS+ stimulus during the recall session. Unlike pupil changes, facial motion tracked each individual FM sweep in the CS+ and CS− stimulus trains and was attenuated—rather than enhanced—at the onset of the CS+ (Figure 1C, right).

Pupil dilation and facial movements were quantified during the initial 4 s of the CS+ and CS− stimulus period during the habituation, conditioning, and recall sessions (Figure 1D). Pupil dilation reflected significant discriminative (Figure 1E) and non-discriminative (Figure 1F) learning on both the conditioning and the recall sessions (statistical reporting provided in the figure legends). Facial motion was unchanged during conditioning and was indiscriminately reduced during recall. Importantly, neither discriminative nor non-discriminative changes in pupil diameter or facial movements were noted in pseudo-conditioned mice (Figure S1).

DTC increases the separability of neural population responses in LA, not HO-AC

To characterize differences in the degree and form of associative plasticity in sensory cortex and the amygdala, we performed simultaneous single-unit recordings from HO-AC and LA during DTC and pseudo-conditioning (Figure 2A). HO-AC recordings targeted a lateral region of the auditory cortex (labeled as AuV in the Allen Brain Institute Atlas or as A2 or SRAF in functional mapping studies).[43–46] Post-mortem reconstructions confirmed targeting of AuV with additional recording sites from the temporal association area (TeA). Here, we operationally defined HO-AC to

Figure 1. Pupil dilation and facial movements index distinct timescales and conditioning specificity during DTC

(A) Schematic illustrating the DTC protocol, where the three sessions are separated by 24 h. In all the sessions, the mice are presented with 15 alternating presentations of a train of frequency-modulated (FM) sweeps in upward or downward direction (conditioned stimulus, CS). Upward sweeps are depicted as the CS+, although assignment of CS+ to sweep direction is counterbalanced across mice. See also Figures S1 and S7.

(B) Left: pupil dilation in each trial is quantified as a fractional change in the pupil diameter (P) relative to the 2 s baseline before CS onset ($\Delta P/P_0$). Right: pupil dilation for all CS presentations (top and middle, n = 15) and mean + SEM across trials (bottom) for all three sessions in an example mouse. Vertical dashed lines denote onset of initial FM sweep, orange bars denote CS duration, and red bars denote the 1 s shock.

(C) Left: facial motion is computed at each time T as the absolute value of the difference in pixel intensities between consecutive frames (T, T + 1) for each pixel and averaged across the region of interest (dashed blue rectangle). Right: facial motion was expressed as a fractional change relative to the pre-CS baseline ($\Delta F/F_0$). Other plotting conventions match those given above.

(D) Left: area under the curve (AUC) was quantified for pupil diameter and facial motion during the first 4 s of the CS period (black rectangle). Right: difference in mean CS+ and CS− AUC for pupil and facial motion during conditioning and recall sessions relative to habituation. Horizontal black bars indicate the mean. Pupil dilations were significantly larger for the CS+ and recall session: repeated-measures two-way ANOVA, n = 20 mice; main effect for stimulus ($F = 14.51$, $p = 0.001$), session ($F = 10.9$, $p = 0.004$), and no significant session × sound interaction ($F = 1.72$, $p = 0.21$). Suppression of facial movements was greater for the CS+ during recall (n = 22 mice): main effects for sound ($F = 9.61$, $p = 0.005$), session ($F = 40.47$, $p < 2 \times 10^{-6}$), and no significant session × sound interaction ($F = 0.02$, $p = 0.88$).

(E) Discriminatory changes reflect differences between CS+ and CS−. Change in pupil diameter and facial motion relative to habituation session (shown above) for CS− was subtracted from CS+. Top: discriminative changes in sound-evoked pupil dilations were larger in conditioning than in recall (repeated-measures ANOVA, main effect for session $F = 6.86$, $p = 0.003$) but were significant in both sessions (one-sample t tests with Bonferroni-Holm correction for multiple comparisons, conditioning, $p = 0.003$; recall, $p = 0.025$). Bottom: no significant discriminatory changes in facial movement were noted (repeated-measures ANOVA, main effect for session $F = 2.28$, $p = 0.12$).

(F) As in (E), but behavioral measures were averaged across CS+ and CS− to assess non-discriminative changes. Top: mean increase in evoked pupil diameter was greater at recall than at conditioning (repeated-measures ANOVA, main effect for session $F = 14.47$, $p = 2 \times 10^{-5}$), but was significant in both sessions (one-sample t tests with Bonferroni-Holm correction for multiple comparisons, conditioning, $p = 0.04$; recall, $p = 0.0002$). Bottom: mean sound-evoked suppression of facial movements was significantly greater at recall than at conditioning (repeated-measures ANOVA, main effect for session $F = 39.68$, $p = 2 \times 10^{-10}$) and was significant at recall but not at conditioning (one-sample t tests with Bonferroni-Holm correction for multiple comparisons, conditioning, $p = 0.08$; recall, $p = 3 \times 10^{-8}$).

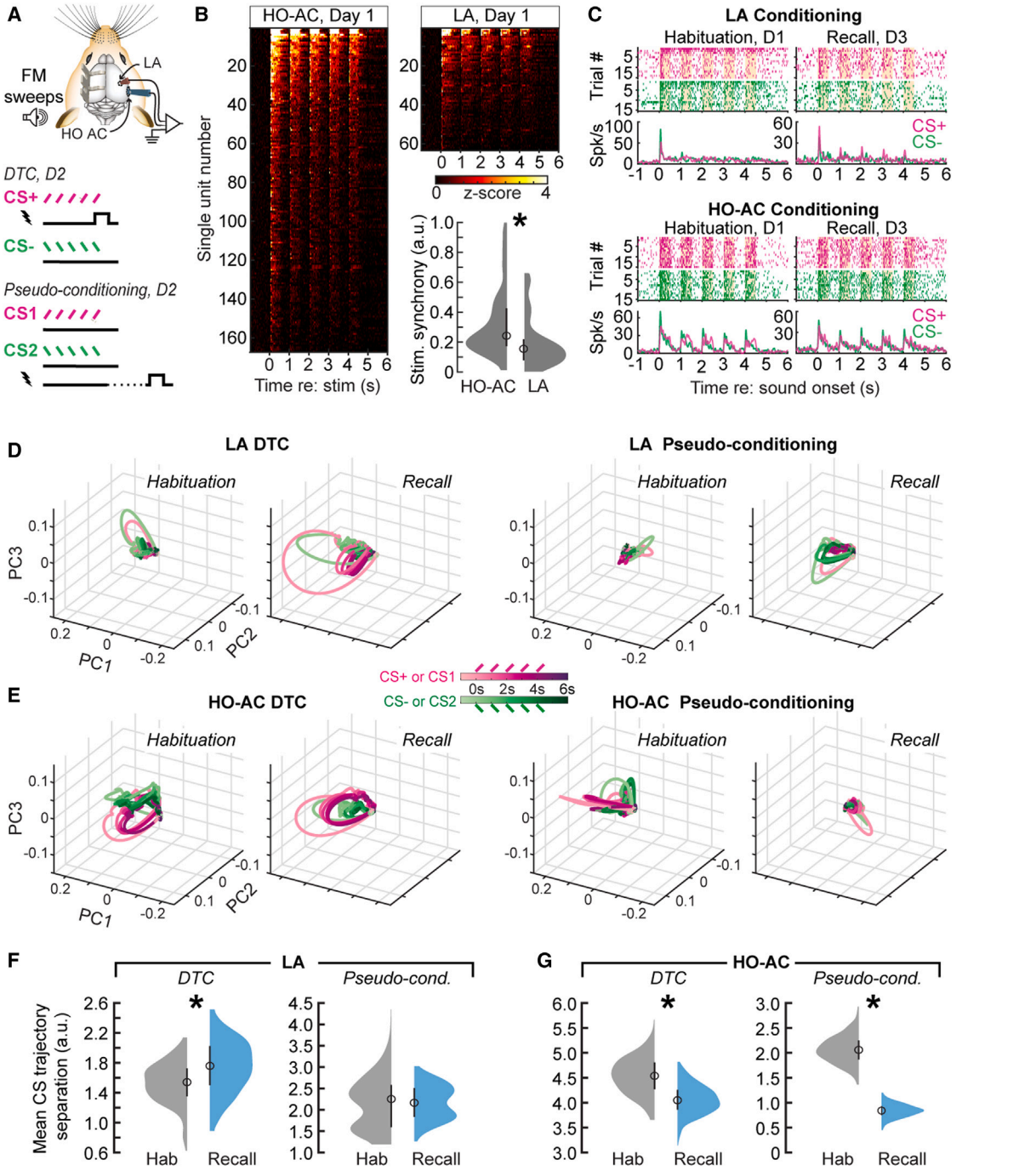

Figure 2. Complex sound representations become more separable after conditioning in LA but less separable over time in HO-AC

(A) Extracellular single-unit recordings were made with two 64-channel probes acutely positioned in the HO-AC and LA on each day of the discriminative threat conditioning (DTC) or pseudo-conditioning procedures. See also Figure S2.

(B) Neurograms showing 167 HO-AC and 63 LA units recorded on the initial session of habituation to the five FM sweeps, 0.5 s in duration, presented at 1 Hz. Neurograms present 1 unit per row, where the spike rate is averaged over 30 upward and downward sweeps and expressed as a *Z* score. HO-AC units synchronized to the FM sweep train with significantly greater fidelity, as evidenced by a significantly greater amplitude of the Fourier transform at 1 Hz (Wilcoxon rank-sum test, p/Cliff's $\delta = 1.41 \times 10^{-5}/-2.655$).

(C) Rastergrams and peri-stimulus time histograms from four example units recorded on the habituation and recall sessions in the LA (top) and HO-AC (bottom).

(D) LA trial-averaged neural population responses throughout a 7 s period surrounding the CS+ and CS− stimulus period are projected on a three-dimensional space defined by the first three principal components (PCs). Stimulus trajectories expand and separate after DTC (left; n mice/n units = 8/49 and 8/110 for

(legend continued on next page)

include AuV and TeA and provide electrode track reconstructions from all mice in Figure S2.

During the initial habituation session, upward and downward FM sweeps elicited responses from both regions, although the native, unconditioned sensory encoding fidelity was greater in the HO-AC, as evidenced by significantly greater synchronization of spike timing to each FM sweep within the 1 Hz stimulus train (Figure 2B). During the recall session, individual units could show disproportionately strong responses to the CS+ (Figure 2C, top) or relatively balanced responses to both CS sounds (Figure 2C, bottom). To measure changes in neural population-level stimulus discriminability before and after DTC, we visualized CS responses as trajectories in a reduced dimensionality space defined by the top three principal components (PCs).[9,47] Before DTC, LA population responses poorly differentiated between the train of upward and downward FM sweeps, reflecting stimulus adaptation and relatively poor synchronization. However, in the post-conditioning recall session, LA population responses displayed an elongated CS+ response trajectory that clearly diverged from the CS− (Figure 2D, left). By contrast, LA response trajectories remained compressed and qualitatively indistinguishable for both habituation and recall sessions in pseudo-conditioned mice (Figure 2D, right). In HO-AC, CS+ and CS− population response trajectories appeared separable in both recording sessions of DTC mice (Figure 2E, left) but became suppressed and poorly distinguished in the recall session of pseudo-conditioned mice (Figure 2E, right). Measuring the Euclidean distance between CS trajectories revealed that LA CS+ and CS− responses were significantly more discriminable in recall sessions compared with habituation in DTC mice but not in pseudo-conditioned controls (Figure 2F). In HO-AC, CS trajectories were more separable during the initial recording session but appeared to habituate and become less separable after DTC or pseudo-conditioning (Figure 2G).

Robust associative plasticity in optogenetically targeted corticoamygdalar projection neurons

On a macroscopic scale, neural signatures of sensory associative learning are reflected in the strength and coherence of functional coupling between multiple brain areas.[4,31,33] These macroscopic changes are enabled by intrinsic and synaptic modifications in specific types of interneurons and projection neurons within local circuits.[48–51] In this regard, blind recordings from single neurons in one brain area (e.g., Figure 2) can be both too precise and not precise enough. Focusing on learning-related changes in one brain area at a time provides no insight into potential changes in the coherence or strength of functional connectivity between simultaneously recorded brain regions. On the other hand, collapsing across genetically or anatomically distinct classes of neurons can obscure highly localized plasticity within particular nodes of functional circuits. To address this point, we sought to expand our focus by studying dynamic changes in functional coupling between HO-AC and LA during DTC, while also narrowing our focus on HO-AC corticoamygdalar (CAmy) projection neurons (Figure 3A).

We first sought to determine the areal and laminar distribution of CAmy neurons within the auditory cortex. This was accomplished by injecting a retrograde tracer, CTB, into the LA (Figure 3B) and documenting the location of labeled neurons in primary regions of the AC (AuP), the ventral AC (AuV), and the temporal association cortex lateral to AC (TeA) (Figures 3C and 3D). CTB-labeled CAmy neurons were more abundant (Figure 3E) and more evenly distributed across layers in AuV and TeA compared with AuP (Figure 3F), confirming that more lateral HO-AC regions provide the bulk of auditory cortical input to LA.

To record from CAmy units, we used an intersectional virus strategy to limit channelrhodopsin (ChR2) expression to HO-AC neurons that project to the amygdala (Figure 3G). HO-AC single units were recorded with translaminar probes (Figure 3H), and we quantified the latency and temporal jitter of spikes evoked by a 1 ms light pulse (Figure 3I). Optogenetically tagged CAmy units were distinguished from indirectly activated HO-AC and LA units based on the strength of evoked spiking (at least 5 SD above baseline), shorter latency of direct vs. polysynaptic activation (less than 5 ms from laser onset), and highly stereotyped spike timing across trials (less than 0.75 ms of jitter; Figure 3J).[14,52,53]

CAmy units showed robust, non-adapting responses to FM sweeps during the habituation session and relatively suppressed responses with disproportionately strong spiking to the CS+ on day 3 recall (Figure 3K). CAmy responses were significantly biased toward the CS+ during recall compared with habituation, matching the relationship observed in LA units but in contrast to neighboring HO-AC units, which did not show a significant CS response bias in either recording session (Figure 3L). CS bias was not observed in LA, HO-AC, or CAmy units in pseudo-conditioned mice (Figure 3M). We noted that the percentage of sound-responsive units in LA doubled in the recall session compared with habituation (34% vs. 17%). This degree of increase was not noted in pseudo-conditioned mice (58 vs. 46 units; Figure 3M), suggesting that the number of sound-responsive LA units could itself be a result of DTC. Finally, CS+ response bias

habituation and recall, respectively) but remain relatively constricted and inseparable for both sessions in pseudo-conditioned mice (right; 3/46 and 3/58 for habituation and recall, respectively). Responses to each FM sweep with the sequence of five stimuli are represented as a distinct trajectory.

(E) Same as in (D), but for HO-AC population responses during the habituation and recall sessions of DTC (n = 8/154 and 8/178 mice/units, respectively) and pseudo-conditioning (n = 3/71 and 3/54, respectively).

(F) Euclidean distance between LA CS+ and CS− population response trajectories averaged over the 5 s CS duration plotted as mean ± SEM (black symbols) of the bootstrapped sample (n = 500 bootstraps) alongside histograms of bootstrapped data (gray and blue for habituation and recall, respectively). CS+ and CS− trajectories were significantly more separable in the recall session compared with habituation in DTC mice (left; unpaired t test, $p < 1 \times 10^{-10}$; Cohen's d = 0.68) but were not significantly changed in pseudo-conditioned mice (right; unpaired t test, p = 0.68; Cohen's d = 0.03).

(G) Plotting conventions match those of (F). HO-AC responses significantly habituate between the two recordings sessions, resulting in significantly less-separable CS trajectories during the recall sessions of both DTC (left; unpaired t test, $p < 1 \times 10^{-10}$; Cohen's d = −1.37) and pseudo-conditioned mice (right; unpaired t test, $p < 1 \times 10^{-10}$; Cohen's d = −5.8).

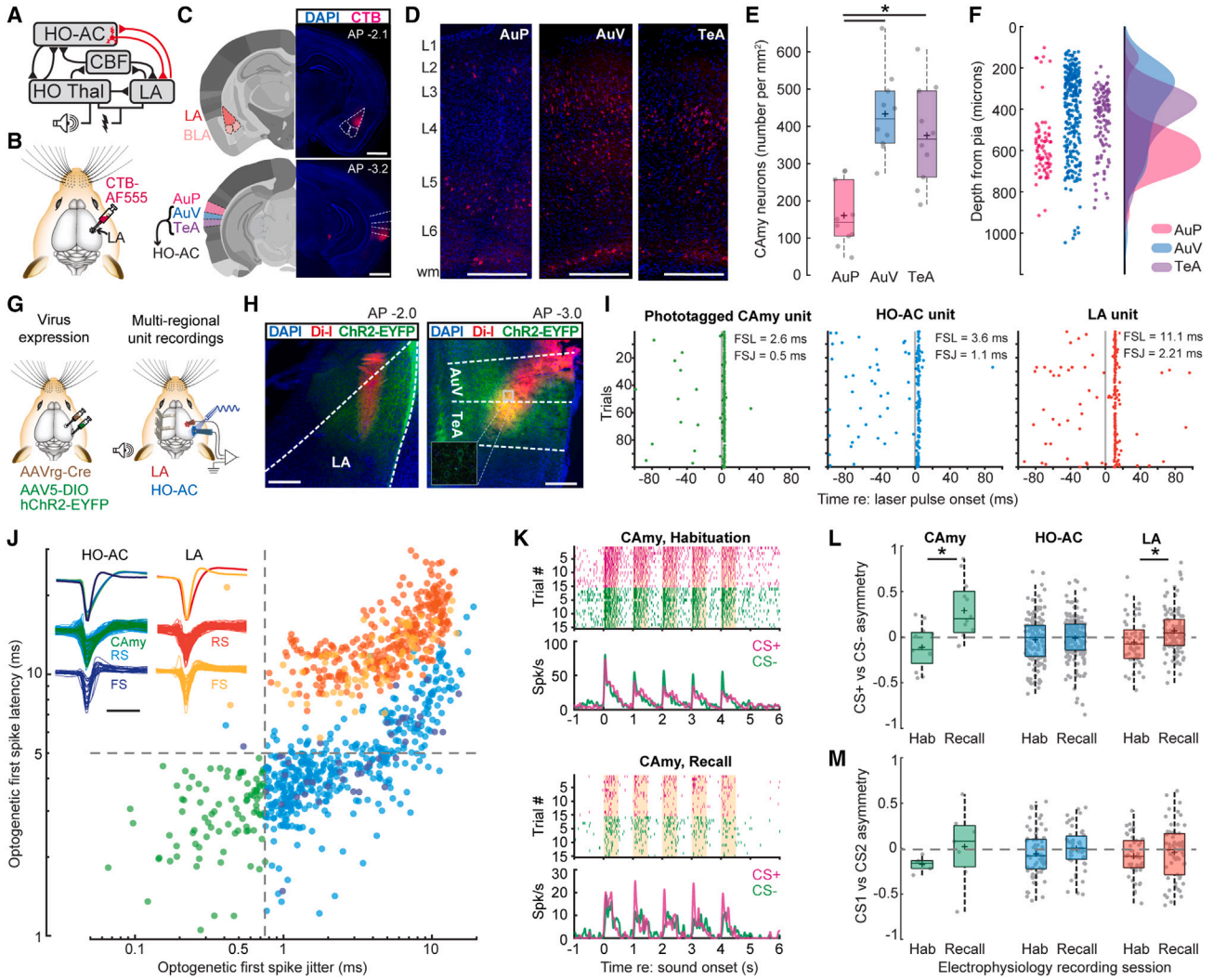

Figure 3. Discriminative plasticity in anatomically and optogenetically targeted HO-AC corticoamygdalar projection neurons resembles LA neurons

(A) Sensory representational plasticity reflecting the association of sound and shock is observed within the higher-order thalamus, cholinergic basal forebrain, auditory cortex, and LA, but is less often studied at the level of isolated classes of corticofugal projection neurons or in the coherent activity between each brain area (illustrated in red).

(B) Cartoon illustrating injection of the fluorescent retrograde tracer CTB-AF555 into the LA.

(C) Coronal sections depicting the caudal portion of the LA targeted for injection (top) as well as the primary region of AC (AuP), ventral AC (AuV), and temporal association area (TeA, bottom). Nomenclature and reference image at left are adapted from the Allen Institute for Brain Science. Here, HO-AC refers to regions denoted as AuV and TeA in the Allen Institute brain reference atlas. Epifluorescence micrographs at right show CTB at the injection site as well as retrogradely labeled corticoamygadalar neurons (CAmy). Scale bar, 1 mm.

(D) Density and laminar distribution of CTB^+ CAmy neurons shown in a higher-magnification confocal image of AuP, AuV, and TeA from the same sections shown in (C). Scale bar, 0.25 mm.

(E) Cell counts demonstrate that CAmy density is greater in AuV and TeA compared with AuP (n = 10/5, slices/mice; repeated-measures ANOVA, F = 16.79, $p = 2 \times 10^{-5}$; *post hoc* pairwise comparisons with Bonferroni-Holm correction for multiple comparisons, AuP vs. AuV, $p = 3 \times 10^{-5}$; AuP vs. TeA, $p = 9 \times 10^{-4}$; AuV vs. TeA, p = 0.30). Box-and-whisker plots show median values in solid black lines, 25th and 75th percentiles, and whiskers extending to the most extreme data points not considered outliers, + indicates the mean.

(F) Distribution of CTB^+ cells in AuP, AuV, and TeA shown in (D) expressed as a function of distance from the pial surface.

(G) Cartoons illustrating strategy for selectively activating CAmy neurons via injection of a retrograde virus encoding Cre-recombinase in the LA and a Cre-dependent virus encoding ChR2-EYFP in HO-AC (left). Multi-channel recording probes are positioned in LA and HO-AC following a virus incubation period, and brief pulses of 473 nm light are presented to the exposed cortical surface with a diode laser to activate $ChR2^+$ CAmy neurons.

(H) Photomicrographs illustrate the Di-I-coated silicon probe insertion trajectory in LA (left) and HO-AC (right). Dashed lines demarcate approximate region borders based on the Allen Brain Institute reference atlas. The somata and neuropil of neurons transduced with both viruses express EYFP. Inset in the right image

(legend continued on next page)

was also not observed in fast-spiking units from either brain region with DTC or pseudo-conditioning, which further emphasizes the cell-type-specific expression of associative plasticity in both brain regions (Figure S3).[14,35,54]

Enhanced corticoamygdalar-evoked local network responses in LA after DTC

Prior work has shown that selective optogenetic inactivation of auditory CAmy axons blocks the behavioral retrieval of threat memory, suggesting that auditory corticofugal projection neurons transmit critical information to the amygdala, particularly for complex auditory CS stimuli.[9] Inspired by an approach that combined optogenetics and local field potential (LFP) recordings to document corticostriatal plasticity supporting learning,[55] we measured the LA LFP response to a brief (1 ms) optogenetic activation of CAmy projection neurons at varying laser powers to test the hypothesis that enhancement of a CAmy-evoked LFP would be evident in the LA following DTC but not pseudo-conditioning (Figure 4A).

Axon terminal expression of ChR2-EYFP in the LA was robust (Figure 3H, left), and optogenetic activation of CAmy cell bodies in HO-AC elicited a monotonic increase in LA LFP amplitude with increasing laser power (Figure 4B). In mice undergoing DTC, CAmy-evoked LFP amplitude was significantly greater during the recall session than the habituation session (Figure 4C), yielding a significantly greater growth slope across laser powers (Figure 4D). No significant changes in CAmy-evoked LA LFP amplitude or growth slopes were noted between the habituation and the recall sessions of mice that underwent pseudo-conditioning (Figures 4E and 4F). Importantly, the optogenetic activation protocol was performed just prior to the interleaved presentation of upward and downward FM sweeps on the habituation and recall sessions, thus highlighting a stabilized potentiation of CAmy efferents that persisted for at least 24 h following DTC.

Asymmetric potentiation of corticoamygdalar inputs during threat memory recall

To test the hypothesis that HO-AC inputs to the LA are enhanced during the recall of threat memory during naturally occurring patterns of neural activity, we measured the LA LFP triggered by HO-AC spiking during the CS presentation period (Figure 5A). The spike-triggered LFP indexes transient changes in the strength and timing of information flow between brain regions[56] and has been used to describe dynamic functional coupling between the amygdala and the pre-frontal cortex,[32] as well as basal forebrain cholinergic neurons and auditory cortex during trace auditory fear conditioning[14] and auditory operant learning.[57] To mitigate noise from other neural sources or other spikes occurring at short intervals, we employed a linear deconvolution method rather than the spike-triggered average.[58]

We noted that HO-AC spikes were associated with negative LFP deflections in LA that peaked 5–10 ms after the cortical spike (Figure 5B). The spike-triggered LFP was equivalent for CS+ and CS− stimuli during the initial habituation session but was specifically enhanced during the CS+ presentation period in the recall session (Figures 5C–5E). Importantly, the sound-evoked LFP amplitude did not differ between CS+ and CS− stimuli in HO-AC or LA, confirming that associative plasticity in the spike-triggered LFP during the CS presentation period cannot be explained solely by bottom-up changes in sound-evoked LFPs (Figure S4).

LA and HO-AC are reciprocally connected.[26–28,59] To determine whether enhanced functional connectivity between the HO-AC and the LA during threat memory is bidirectional or asymmetric, we calculated the spike-triggered LFP from LA to HO-AC (Figure 5F). We noted that negative deflections in cortical LFPs peaked several milliseconds following LA spikes, confirming that the relatively sparse population of corticopetal projections from the LA could be studied with our functional connectivity assay (Figure 5G). However, we did not observe a systematic difference in the spike-triggered LFP amplitude between CS+ and CS− stimuli in either recording session (Figures 5H–5J). Further, discriminative plasticity in the spike-triggered LFP was not observed in pseudo-conditioned mice (Figure S5), emphasizing that enhanced functional connectivity was specific to the CS+, specific to DTC, specific to recall, and observed only for descending corticofugal projections.

Discriminative changes in amygdalar ACh release

Measurements of acetylcholine (ACh) microdialysis suggested a "slow and tonic" role wherein the cholinergic basal forebrain was recruited by brain-stem and midbrain arousal centers to produce

depicts a small region of interest photographed at higher magnification with a confocal microscope to illustrate somatic expression of ChR2-EYFP. Scale bar, 0.25 mm.

(I) Spike rasters from a photo-tagged CAmy unit and regular spiking (RS) single units in HO-ACtx and LA in response to the 1 ms laser pulse stimulation. Gray vertical line denotes onset of 1 ms laser pulse. FSL, first spike latency; FSJ, first spike jitter.

(J) Inset: HO-AC and LA single units were classified as RS or fast spiking (FS) (trough-to-peak delay $\geq$ 0.6 ms or <0.6 ms, respectively). Mean waveform shapes are shown on the top row; waveforms from all units are shown in the bottom two rows. Scale bar, 1 ms. CAmy units (green) were operationally defined as HO-AC RS units with a low first spike latency (<5 ms, dashed horizontal line) and a low first spike jitter (<0.75 ms, dashed vertical line) in response to 1 ms laser pulse stimulations. All other RS and FS units in HO-AC and LA are also plotted for comparison.

(K) Rastergrams and peri-stimulus time histograms from two example CAmy units recorded on the habituation and recall sessions.

(L) Discriminative plasticity from sound-responsive units in eight DTC mice using an asymmetry index ([CS+ − CS−]/[CS+ + CS−]), where positive values reflect a greater response to the CS+, negative values to the CS−, and a value of zero reflects an equivalent response to both stimuli. CS-evoked responses were significantly biased toward the CS+ in the recall session compared with habituation in LA RS units (n = 49/110 units in habituation/recall; unpaired t test, p = 0.003, Cohen's d = 0.51) and optogenetically photo-tagged HO-AC CAmy units (n = 12/12; p = 0.002, Cohen's d = 1.44), but not HO-AC in RS units that were not identified as CAmy units (n = 142/166; p = 0.59, Cohen's d = 0.06).

(M) Discriminative plasticity from sound-responsive units in three mice that underwent pseudo-conditioning with the same analysis described above. Responses to upward and downward FM sweeps (CS1, CS2) did not show a significant difference in bias in LA RS units (n = 46/58 units in habituation/recall; unpaired t test, p = 0.43, Cohen's d = 0.16), optogenetically photo-tagged HO-AC CAmy units (n = 6/7; p = 0.29, Cohen's d = 0.62), or HO-AC RS units not identified as CAmy units (n = 65/47; p = 0.22, Cohen's d = 0.24). See also Figure S3.

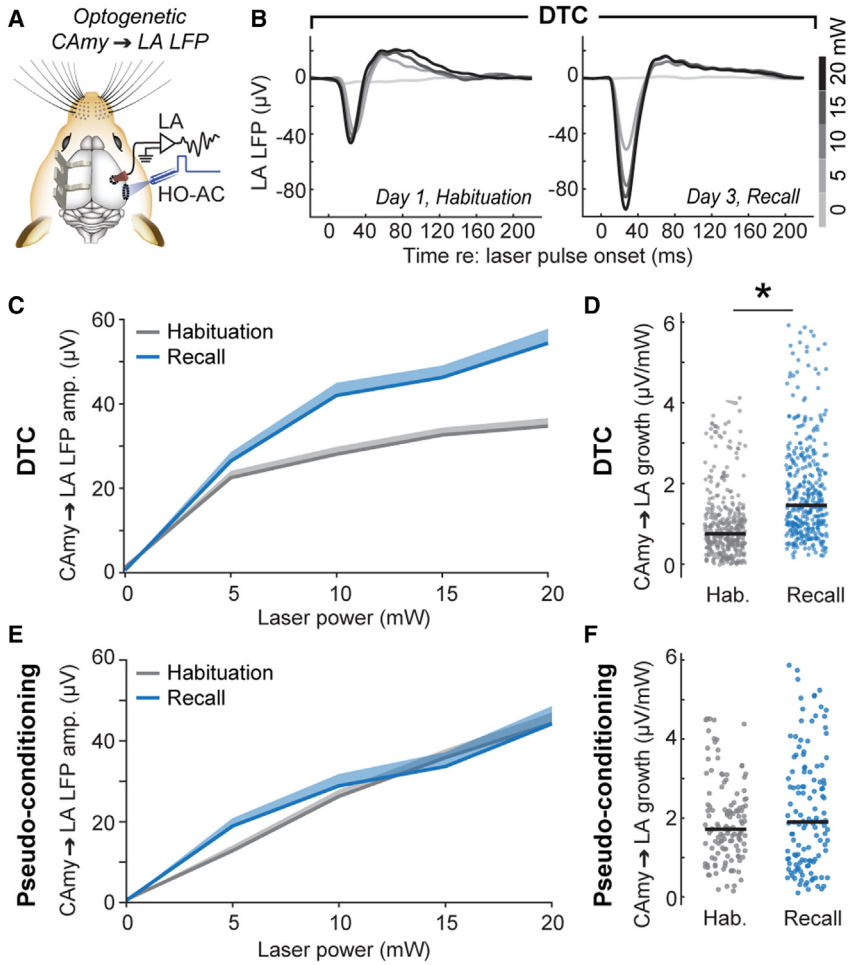

Figure 4. Potentiation of corticoamygdalar-evoked LA activity after discriminative threat conditioning

(A) Cartoon illustrating the protocol for LA local field potential (LFP) recordings during bulk optogenetic stimulation of HO-AC CAmy neurons.

(B) Optogenetically evoked LFPs in the LA of an example DTC mouse for different laser intensities, shown for habituation and recall days.

(C) Mean + SEM LFP amplitude as a function of laser power in the example DTC mouse (B) during habituation and recall.

(D) Slope of light-evoked response growth functions for all channels in DTC mice (n = 6/384, mice/channels). Horizontal black bars indicate the median. Asterisk indicates statistical significance with Wilcoxon rank-sum test (p/Cliff's $\delta = 2 \times 10^{-30}/0.48$).

(E) As in (C), but in an example pseudo-conditioned control mouse.

(F) As in (D), but in pseudo-conditioned controls (n = 2/128, mice/channels). No significant change in the response growth prior to recall compared with habituation; Wilcoxon rank-sum test (p/Cliff's δ = 0.46/0.05).

temporally slow (i.e., minutes) and spatially diffuse (i.e., hundreds of micrometers) changes in cortical ACh release across varying states of sleep and wakefulness (for review, see Jiménez-Capdeville and Dykes,[60] Steriade,[61] and Yu and Dayan[62]). Higher-resolution techniques now show that cholinergic basal forebrain neurons also act locally and phasically, on time scales ranging from milliseconds to tens of seconds to regulate perceptual salience across waking states (for review, see Disney and Higley,[63] McGinley et al.,[64] and Sarter and Lustig[65]). Direct recordings of endogenous ACh release via genetically encoded fluorescent ACh sensors or cholinergic neural activity demonstrate that cholinergic inputs to LA or HO-AC function like teaching signals, on account of their short-latency phasic responses to auditory stimuli that are rapidly and discriminatively rescaled when they predict primary behavioral reinforcers.[14–16] This raises the possibility that CS sounds might elicit endogenous ACh release in both brain structures and that the amplitude of ACh release could be discriminatively modified early in the DTC process, even during the conditioning session.

While tail shock electrically interfered with our ability to analyze electrophysiology data from the conditioning session, we were able to measure ACh dynamics throughout all stages of the DTC procedure via simultaneous dual optic fiber recordings of the $GRAB_{ACh}3.0$ fluorescent sensor (ACh3.0; Figure 6A) in LA (Figure 6B) and HO-AC (Figure 6C).[66] Optic fiber tip placements successfully targeted LA and HO-AC, as shown in fiber reconstructions from six mice that contributed dual-fiber photometry data (Figure S6). To leverage the advantages of fiber photometry for stable long-term recordings and to capture ACh dynamics with greater sensitivity during threat memory acquisition, we extended the habituation phase of the DTC procedure to 2 days and the conditioning phase to 3 days. A final post-conditioning session on day 6 provided an assay for threat memory recall. Combined pupillometry and facial videography in all sessions confirmed the same pattern of changes observed with a 3-day protocol; namely, pupil dilation captured associative memory for the CS+ during conditioning and recall, whereas sound-evoked facial movements were more equivalently suppressed for CS+ and CS− stimuli (Figure S7).

In the first session, we noted robust sound-evoked ACh release in both LA (Figure 6D) and HO-AC (Figure 6E). In HO-AC, sound-evoked cholinergic responses were reduced between habituation sessions, in line with prior reports of strong habituation to stimulus novelty (Figures 6E and 6F).[15] We noted a striking divergence in sound-evoked ACh release between brain regions. In LA, CS-evoked responses increased across conditioning and recall sessions, particularly for the CS+ (Figure 6G, top), paralleling the LA neural population responses measured during recall (Figures 2D and 2F). By contrast, HO-AC ACh release strongly habituated over time for both the CS+ and the CS− (Figure 6G, bottom), again paralleling the net reduction in stimulus discriminability noted in HO-AC population responses (Figures 2E and 2G). During conditioning, we found

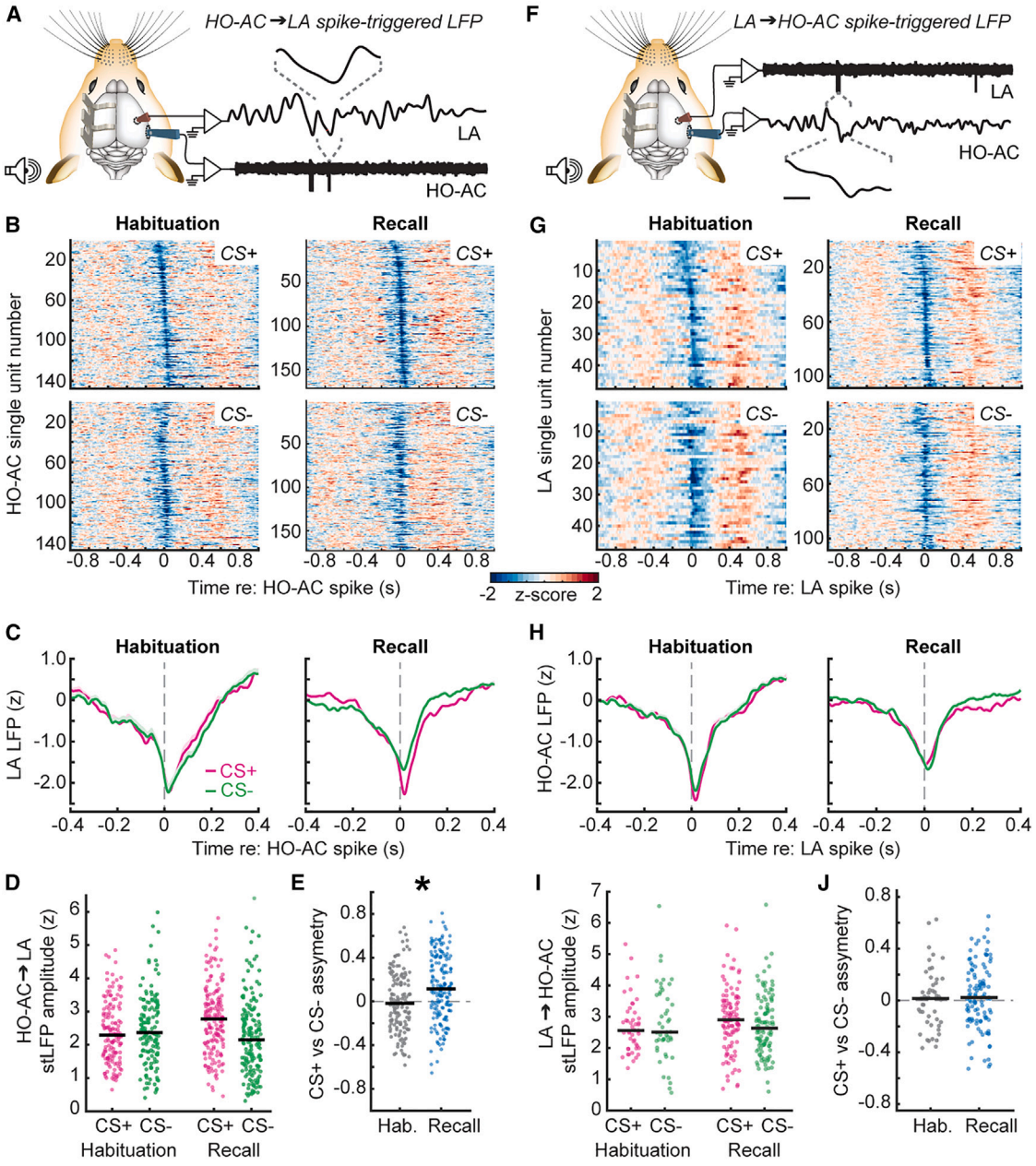

Figure 5. Enhanced functional coupling from HO-AC to LA—but not LA to HO-AC—during threat memory recall

(A) Schematic illustrating the quantification of LA LFPs triggered by HO-AC single-unit spikes. Linear deconvolution by time expansion is used to estimate the spike-triggered LFP (stLFP).

(B) HO-AC to LA stLFPs computed during the CS+ (top) and CS− (bottom) expressed as a *Z* score relative to pre-stimulus baseline and averaged across all LA recording channels.

(C) Mean + SEM HO-AC to LA stLFP demonstrates a downward deflection of the LA LFP shortly following HO-AC spikes that is selectively enhanced for the CS+ during the recall session.

(D) LA stLFP amplitude for each HO-AC RS unit during each CS presentation on habituation and recall sessions (n = 8/147, 8/171 mice/units for habituation and recall, respectively). Horizontal black bars indicate the mean. LA stLFP is significantly and specifically elevated during CS+ stimuli after DTC: mixed-model ANOVA with session as a factor and sound as a repeated measure, main effect for session ($F = 0.86$, $p = 0.35$), main effect for sound ($F = 8.88$, $p = 0.003$), session × sound interaction term ($F = 15.43$, $p = 0.0001$).

(E) Discriminative plasticity in the HO-AC to LA stLFP expressed as an asymmetry index ([CS+ − CS−]/[CS+ + CS−]), where positive values reflect a greater response to the CS+ and negative values to the CS−, and a value of zero denotes an equivalent response. CS+ bias was significantly greater than zero in the recall session (one-sample t test, $p = 8 \times 10^{-7}$; Cohen's d = 0.41) and significantly greater than the habituation session (unpaired t test, p/Cohen's d = 0.0002/0.44). Horizontal black bars indicate the mean.

(legend continued on next page)

enhanced ACh release for the CS+ relative to the CS− (Figure 6H, top), but did not find discriminative changes in HO-AC. Although opposite in sign—increased in LA, decreased in HO-AC—average CS-evoked ACh was significantly changed during the conditioning and recall sessions for both brain regions (Figure 6I).

Neurophysiological predictors of threat memory strength

Taken together, these findings show that cholinergic and corticofugal inputs convey sensory information to the LA and—like higher-order thalamic inputs[18–20]—are themselves sites of upstream plasticity that may guide associative plasticity processes within the amygdala (Figure 6J). To investigate the relationship between neurophysiological plasticity and threat memory strength, we correlated each plasticity measure with changes in pupil dilation and facial motion in individual mice. Above, we reported above that CS-evoked pupil dilations provided a stronger index of discriminative memory than CS-evoked facial movements (Figure 1) and that CS-evoked LA firing rates (Figure 3), corticofugal functional coupling (Figure 5), and LA ACh release (Figure 6) showed the strongest discriminative plasticity. Correspondingly, we found that LA firing rates, corticofugal coupling, and LA ACh release during recall were all moderately predictive (R^2 0.21 to 0.43) of individual changes in CS+-evoked pupil dilations (Figure 7A, top row), whereas HO-AC firing rate changes, corticopetal functional coupling, or HO-AC ACh release were not (R^2 0.01 to 0.15). By contrast, LA firing rates, corticofugal coupling, and LA ACh release were less predictive of changes in CS−-evoked pupil dilations (R^2 0 to 0.38; Figure 7A, bottom row). LA ACh release was somewhat predictive of CS+-evoked changes in facial motion (R^2 0.28 to 0.34; Figure 7B), but the remaining physiological measures were not (R^2 0.01 to 0.16; Figure 7B). Across all permutations of neural and motor measurements, only HO-AC spikes associated with LA field potentials were significantly predictive of pupil-indexed threat memory (Figure 7C), suggesting that changes in CAmy descending functional connectivity may capture some of the same interanimal variability in threat memory strength as reported previously in incertocortical and geniculocortical projections.[20,36]

DISCUSSION

Across animal models and conditioning protocols, there is strong overall evidence for a rapid and persistent modification of LA responses to enhance the salience of sounds that predict aversive reinforcement.[1,2] Selective enhancement of CS+ representations following DTC has been reported in the auditory cortex,[21] although cortical receptive field plasticity is less consistent overall than LA and depends—as we have shown here—on the cortical cell type and auditory cortex region,[9,34] the degree of non-discriminative vs. specific fear learning,[67,68] and the use of complex auditory CS stimuli or more complex conditioning protocols[9,14,35] and has been interpreted as reflecting attentive processing of threatening stimuli rather than their short latency sensory feature encoding.[69]

We noted a selective enhancement of the CS+ representation in LA population responses and regular spiking unit firing rates but not in HO-AC population responses or single-unit firing rates. Discriminative plasticity in CAmy units, by contrast, was more akin to LA units than to neighboring units in HO-AC, in that they also exhibited a selective enhancement of CS+ responses. These findings can be explained by a dual-stream model, which purports that the auditory thalamus and cortex feature intermingled functional populations of highly plastic neurons that reflect the learned significance of environmental sounds (e.g., CAmy projection neurons) alongside other populations that are optimized for stable encoding of environmental stimuli based on their physical features and overall novelty independent of fear associations.[70,71] Another possibility is that unidentified regular- and fast-spiking units that—on average—did not exhibit discriminative enhancement of the CS could nevertheless encode associative threat memory at more remote time points than the next-day recall session used here.[28,33,72] A third possibility is that most HO-AC neurons do encode the discriminative threat memory at the timescale studied here, but the representation of the memory is not based in overall changes in firing rate but instead in the stability of neurons that are functionally connected into CS+ and CS− ensembles.[9,19,68,73]

Interregional functional coupling and asymmetric potentiation of corticofugal plasticity

The LA and HO-AC are reciprocally interconnected, where the HO-AC both sends and receives approximately three times more input with the LA than primary auditory cortex, as shown here and in prior work.[7,27,28,74,75] We used the spike-triggered LFP to demonstrate that the reciprocal anatomical connectivity between HO-AC and LA mirrored functional reciprocity, such that a spike in either region was associated with the maximal negativity in the LFP 5–10 ms later, the temporal lag suggesting that the major contributor is the interarea communication rather than shared common inputs. The directional coordination between the output (spikes) of one region and the input (LFPs) of another brain region is thought to facilitate learning and memory of salient information by reducing intertrial variability and increasing post-synaptic excitability, thereby allowing for more efficient information transfer.[32]

Sensory corticofugal neurons innervate far-flung targets in the forebrain, midbrain, and brain stem, and their plasticity can shape real-time processing and regulate long-term plasticity of sensory representations in downstream subcortical targets.[76–79] Despite the symmetry in the functional connectivity between

(F–H) As in (A–C), but for the HO-AC LFP triggered by spikes in individual LA units.

(I) Plotting conventions match those of (D). HO-AC stLFP amplitude for each LA unit (n = 8/47, 8/108 mice/units for habituation and recall, respectively). Horizontal black bars indicate the mean. No significant changes were observed: mixed model ANOVA with session as a factor and sound as a repeated measure, main effect for session ($F = 0.52$, $p = 0.47$), main effect for sound ($F = 0.28$, $p = 0.6$), session × sound interaction term ($F = 1.57$, $p = 0.21$).

(J) Plotting conventions match those of (E). LA to HO-AC stLFP amplitude was not biased toward the CS+ during recall (one-sample t test, $p = 0.62$, Cohen's $d = 0.12$) nor different from habituation measures (unpaired t test, p/Cohen's $d = 1.29/0.08$). Horizontal black bars indicate the mean. See also Figures S4 and S5.

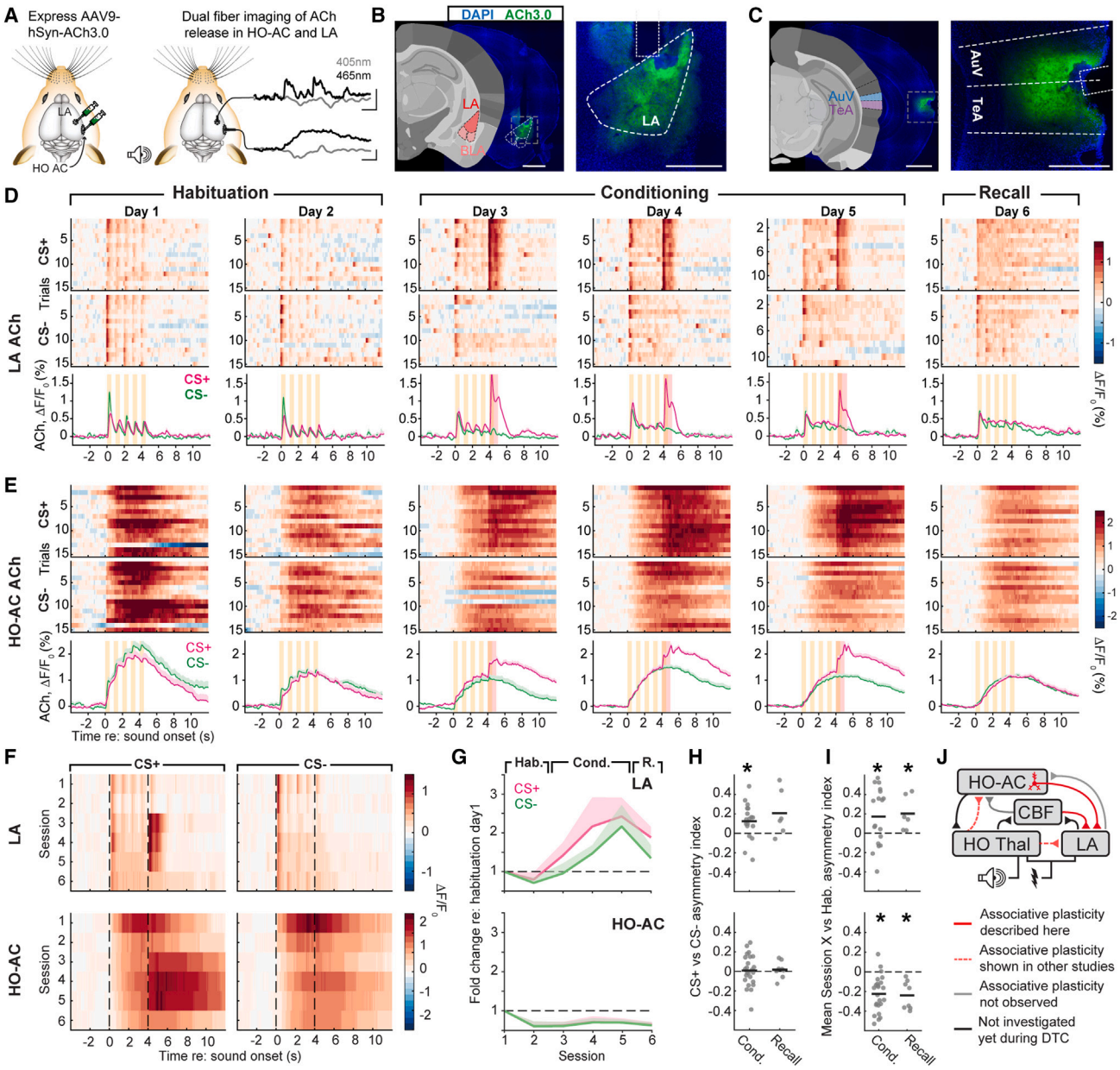

Figure 6. Discriminative and non-discriminative changes in sound-evoked acetylcholine release begin during threat conditioning

(A) Left: Schematic illustrating viral expression of the genetically encoded fluorescent ACh sensor, ACh3.0. Right: Simultaneous fiber-based bulk fluorescence measurements in the LA and HO-AC at the ACh3.0 excitation wavelength (465 nm) and a control wavelength (405) that is not sensitive to ACh release. Vertical and horizontal bars represent 1% ΔF and 2 s, respectively.

(B) Coronal sections depicting the LA region targeted for injection (left). Nomenclature and reference image are adapted from the Allen Institute for Brain Science. Fluorescence micrographs show ACh3.0 expression and estimated position of the optic fiber (dotted white line), and approximate region borders (dashed white line). Scale bars, 1 mm (left) and 0.5 mm (right). See also Figure S6.

(C) As in (B), but for HO-AC. Scale bars, 1 mm (left) and 0.5 mm (right).

(D) The fractional change in ACh3.0 reveals phasic ACh release in LA elicited by each FM sweep (yellow rectangle) and tail shock (red rectangle). LA ACh release for each CS+ and CS− trial and mean + SEM across trials (bottom) for each session in an example mouse. For fiber imaging experiments, the habituation phase is extended to 2 days and the conditioning phase to 3 days. See also Figure S7.

(E) As in (D), but for HO-AC recorded in the same mouse simultaneously.

(F) Mean trial-averaged fractional change for each recording session across six dual-implant mice. Dashed vertical lines denote the 4 s CS period prior to onset of the fifth FM sweep and tail shock used to calculate the CS+ and CS− response values.

(G) Mean + SEM fold change in CS+ and CS− evoked activity during the initial 4 s stimulus period expressed relative to the first habituation session in six dual-implant mice. In LA (top), sound-evoked cholinergic responses increase throughout conditioning and recall but do not systematically differ by CS type: two-way

(legend continued on next page)

HO-AC and LA, only the corticofugal—and not corticopetal—functional coupling exhibited discriminative plasticity and was significantly predictive of pupil-indexed threat memory. The asymmetric potentiation in CAmy influence on LA ensembles reinforces inactivation studies showing the necessary involvement of HO-AC CAmy projections in the recall of short-term threat memory with complex sounds,[9] in the recall of remote auditory threat memories,[33,72] and in the reacquisition of additional auditory threat associations.[33,72] Future work is needed to address whether the asymmetric CS+ response potentiation in CAmy neurons is distinct from other projection neuron types across the cortical column. One possibility is that, compared with other pyramidal neuron types, CAmy apical dendrites may have privileged synaptic connectivity with interneurons and higher-order incertocortical and geniculocortical afferents in layer 1, which provides a pre-synaptic basis for conferring strong discriminative enhancement of the CS+ representation.[20,29,34,36]

Sound-evoked ACh release and plasticity in LA and HO-AC

We observed that FM sounds with no learned relevance evoked strong ACh release in both HO-AC and LA during the initial habituation session. Apart from that similarity, ACh3.0 response kinetics and plasticity differed in nearly every way in the two brain regions (phasic, discriminative, and generally potentiating in LA, while more sluggish and non-discriminatively suppressed in HO-AC). The underlying mechanisms for differences in temporal response profiles are unknown, but could reflect varying response properties of cholinergic afferents, different expression levels of acetylcholinesterase, or different levels of ACh3.0 expression within each area. With bulk fiber imaging, transduced neurons within the cone of light contribute to the measured signal. Given the numerical aperture and diameter of the flat-tipped fibers used here for LA imaging, fluorescence from brain regions ~0.2 mm below the fiber tip provide the greatest contribution to the measured signal.[80] While some AAV-ACh3.0 expression was observed outside of LA, it was fairly well localized to LA (Figure S6) and—more importantly—because all fibers were well above the ventral boundary of LA, ACh inputs to the basal lateral nucleus are unlikely to contribute to the signals measured here.

Limitations of the study

Future work using targeted inactivation methods is needed to address whether potentiated corticofugal and cholinergic inputs to LA are instructive signals that guide and maintain amygdalar plasticity or whether they constitute a redundant encoding of memory distributed over distant brain regions. Also, we did not perform ACh3.0 measurements in a separate cohort of pseudo-conditioned mice. However, the fact that ACh release differed in every way between the LA and the HO-AC is itself an internal control that argues against the involvement of an extraneous brain-wide contribution related to movement or another source of artifact. Second, the 405 nm control wavelength captured signal variations unrelated to ACh release and was subtracted from the ACh3.0 sensor fluorescence signal. However, we cannot rule out the possibility that a global reduction in signal-to-noise ratio could have contributed to the strong and non-specific habituation in sound-evoked ACh release in HO-AC.

STAR★METHODS

Detailed methods are provided in the online version of this paper and include the following:

- KEY RESOURCES TABLE
- RESOURCE AVAILABILITY
  - Lead contact
  - Materials availability
  - Data and code availability
- EXPERIMENTAL MODEL AND SUBJECT DETAILS
  - Animal subjects
- METHOD DETAILS
  - Surgical preparation
  - Head plate attachment
  - Injections and fiber implantation
  - Electrophysiology
  - Fiber photometry
  - Discriminative threat conditioning
  - Pupillometry and facial videography
  - Histology
- QUANTIFICATIONS AND STATISTICAL ANALYSIS
  - Electrophysiology data acquisition

repeated-measures ANOVA, main effect for session ($F = 5.08$, $p = 0.002$), main effect for sound ($F = 3.11$, $p = 0.14$), session × sound interaction term ($F = 0.7$, $p = 0.63$). In HO-AC (bottom), sound-evoked cholinergic responses decrease throughout conditioning and recall but do not systematically differ by CS type: two-way repeated-measures ANOVA, main effect for session ($F = 4.5$, $p = 0.003$), main effect for sound ($F = 0.07$, $p = 0.8$), session × sound interaction term ($F = 0.03$, $p = 0.99$).

(H) Differences in evoked responses by the CS+ and CS− are calculated from the response to each stimulus for a given conditioning or recall session relative to the mean of the two habituation sessions. Discriminative plasticity is computed as an asymmetry index ([CS+ − CS−]/[CS+ + CS−]), where a positive value denotes a greater response to the CS+. Circles denote the trial-averaged mean for a single session from a single mouse. Horizontal black lines denote sample mean. In LA (top), cholinergic responses were significantly biased toward the CS+ during the conditioning sessions (one-sample t test relative to a population mean of 0, $p = 0.01$, Cohen's $d = 0.68$, $n = 18$) and during the recall session ($p = 0.09$, Cohen's $d = 0.87$, $n = 6$). Significant discriminatory changes were not observed in HO-AC (bottom; $p > 0.58$ and Cohen's $d < 0.21$ for both conditioning and recall, $n = 18$ and 6, respectively).

(I) As in (H), but CS-evoked responses were averaged across CS+ and CS− to provide a measure of overall mean changes over threat memory acquisition and retrieval. Non-discriminative plasticity is computed as an asymmetry index ([session X − $\text{habituation}_{\text{mean}}$]/[session X + $\text{habituation}_{\text{mean}}$]) where a positive value denotes the mean CS response as greater than habituation. In LA (top), CS-evoked cholinergic responses were significantly increased relative to habituation in both conditioning and recall ($p < 0.04$ and Cohen's $d > 0.58$ for both time points). In HO-AC (bottom), CS-evoked cholinergic responses were significantly reduced relative to habituation in both conditioning and recall ($p < 0.002$ and $|\text{Cohen's } d| > 1.23$ for both time points).

(J) Summary diagram illustrating afferent pathways to the LA shown here to be discriminatively modified during the acquisition, consolidation, or recall of threat memory (solid red). Other projection pathways shown in other work to be discriminatively modified during DTC are shown in dashed red. Gray lines denote pathways studied here that did not exhibit discriminative plasticity. Black denotes pathways yet to be investigated during DTC.

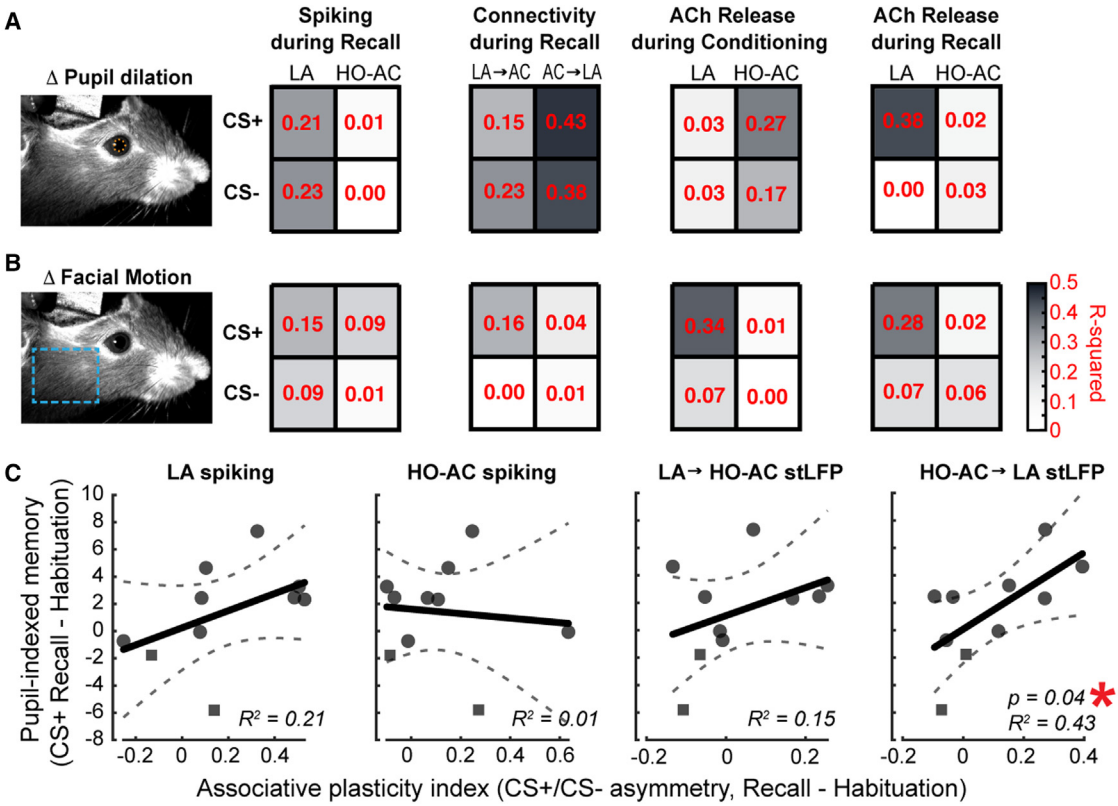

Figure 7. Neurophysiological predictors of threat memory strength

(A) Associative plasticity in CS-evoked spiking, functional connectivity, and ACh release was expressed by first calculating an average asymmetry index ([CS+ − CS−]/[CS+ + CS−]) for each session. The average asymmetry index from the conditioning or recall sessions was calculated relative to the habituation session, by subtracting the habituation value, such that more positive values indicated a greater strengthening of CS+ responses. Changes in CS+ and CS−-evoked pupil dilations relative to the habituation session were then regressed on each associative plasticity index across individual mice for each area (spiking, connectivity, ACh release during conditioning and recall). The proportion of the variation in pupil dilation change that is predictable from the associative plasticity measure is expressed for each combination as the R^2 value. Changes in ACh release during conditioning were obtained from the third session only, where associative plasticity pupil-indexed memory was most pronounced.

(B) As in (A), but for changes in sound-evoked facial movements.

(C) Scatterplots with 95% confidence bounds (dashed lines) and linear regression line (solid black) for four linear regression analyses shown above. Measurements were obtained from dual silicon probe recordings and pupillometry in eight mice that underwent DTC (circles) and two mice that underwent the pseudo-conditioning procedure (squares). Asterisk denotes a statistically significant prediction of pupil-indexed memory from discriminative changes in corticofugal functional connectivity.

- Single unit identification and analyses
- Neural population trajectories
- Local field potential extraction and analyses
- Photometry signal pre-processing and analyses
- Pupil dilation response
- Facial motion response
- Analysis of brain sections
- Statistical analysis

SUPPLEMENTAL INFORMATION

Supplemental information can be found online at https://doi.org/10.1016/j.celrep.2023.113167.

ACKNOWLEDGMENTS

We thank Liam Casey, Ashwini Melkote, Ke Chen, Christine Liu, Sam Smith, and Anne Takesian for technical guidance. We thank Yulong Li for making the $GRAB_{ACh}3.0$ sensor available for purchase. Financial support was provided to D.B.P. by the Nancy Lurie Marks Family Foundation and NIH grants DC009836 (for electrophysiology experiments) and DC017078 (for cholinergic fiber photometry experiments). E.Y.K. was supported by NIH grant MH116135.

AUTHOR CONTRIBUTIONS

Conceptualization, M.M.A. and D.B.P.; methodology, M.M.A., Y.W., E.Y.K., and D.B.P.; investigation, M.M.A. and Y.W.; software, M.M.A. and E.Y.K.; formal analysis, M.M.A.; data curation, M.M.A.; visualization, M.M.A. and D.B.P.; writing – original draft, M.M.A. and D.B.P.; writing – review & editing, M.M.A., E.Y.K, and D.B.P.; resources, D.B.P.; supervision, D.B.P.; funding acquisition, D.B.P.

DECLARATION OF INTERESTS

The authors have no competing interests to declare.

Received: February 1, 2023
Revised: July 7, 2023
Accepted: September 7, 2023
Published: September 23, 2023

REFERENCES

1. Janak, P.H., and Tye, K.M. (2015). From circuits to behaviour in the amygdala. Nature, 284–292. https://doi.org/10.1038/NATURE14188.
2. LeDoux, J. (2007). The amygdala. Curr. Biol. *17*, R868–R874. https://doi.org/10.1016/J.CUB.2007.08.005.
3. Maren, S., and Quirk, G.J. (2004). Neuronal signalling of fear memory. Nat. Rev. Neurosci. *5*, 844–852.
4. Herry, C., and Johansen, J.P. (2014). Encoding of fear learning and memory in distributed neuronal circuits. Nat. Neurosci. *17*, 1644–1654.
5. Tovote, P., Fadok, J.P., and Lüthi, A. (2015). Neuronal circuits for fear and anxiety. Nat. Rev. Neurosci. *16*, 317–331.
6. Ledoux, J.E., Farb, C., and Ruggiero, D.A. (1990). Topographic Organization of Neurons in the Acoustic Thalamus That Project to the Amygdala. J. Neurosci. *10*, 1043–1054.
7. Romanski, L.M., and Ledoux, J.E. (1993). Information Cascade from Primary Auditory Cortex to the Amygdala: Corticocortical and Corticoamygdaloid Projections of Temporal Cortex in the Rat. Cerebr. Cortex *3*, 515–532. https://doi.org/10.1093/CERCOR/3.6.515.
8. Barsy, B., Kocsis, K., Magyar, A., Babiczky, Á., Szabó, M., Veres, J.M., Hillier, D., Ulbert, I., Yizhar, O., and Mátyás, F. (2020). Associative and plastic thalamic signaling to the lateral amygdala controls fear behavior. Nat. Neurosci., 625–637. https://doi.org/10.1038/s41593-020-0620-z.
9. Dalmay, T., Abs, E., Poorthuis, R.B., Hartung, J., Pu, D.L., Onasch, S., Lozano, Y.R., Signoret-Genest, J., Tovote, P., Gjorgjieva, J., et al. (2019). A Critical Role for Neocortical Processing of Threat Memory. Neuron *104*, 1180–1194. https://doi.org/10.1016/J.NEURON.2019.09.025/ATTACHMENT/50079C60-1BC6-48C5-AA20-0E7731E52346/MMC2.XLSX.
10. Gielow, M.R., and Zaborszky, L. (2017). The Input-Output Relationship of the Cholinergic Basal Forebrain. Cell Rep. *18*, 1817–1830. https://doi.org/10.1016/J.CELREP.2017.01.060/ATTACHMENT/F4BFC68F-51A3-4A56-9EC9-43DC12BF6F69/MMC4.MP4.
11. Woolf, N.J., and Butcher, L.L. (1982). Cholinergic projections to the basolateral amygdala: A combined Evans Blue and acetylcholinesterase analysis. Brain Res. Bull. *8*, 751–763. https://doi.org/10.1016/0361-9230(82)90102-2.
12. Mesulam, M.M., Mufson, E.J., Wainer, B.H., and Levey, A.I. (1983). Central cholinergic pathways in the rat: An overview based on an alternative nomenclature (Ch1–Ch6). Neuroscience *10*, 1185–1201. https://doi.org/10.1016/0306-4522(83)90108-2.
13. Hegedüs, P., Sviatkó, K., Király, B., Martínez-Bellver, S., and Hangya, B. (2023). Cholinergic activity reflects reward expectations and predicts behavioral responses. iScience *26*, 105814. https://doi.org/10.1016/j.isci.2022.105814.
14. Guo, W., Robert, B., and Polley, D.B. (2019). The Cholinergic Basal Forebrain Links Auditory Stimuli with Delayed Reinforcement to Support Learning. Neuron *103*, 1164–1177. https://doi.org/10.1016/J.NEURON.2019.06.024/ATTACHMENT/FD65952D-C73B-45BE-9745-C0D4C200D429/MMC1.PDF.
15. Robert, B., Kimchi, E.Y., Watanabe, Y., Chakoma, T., Jing, M., Li, Y., and Polley, D.B. (2021). A functional topography within the cholinergic basal forebrain for encoding sensory cues and behavioral reinforcement outcomes. Elife *10*, e69514. https://doi.org/10.7554/ELIFE.69514.
16. Crouse, R.B., Kim, K., Batchelor, H.M., Girardi, E.M., Kamaletdinova, R., Chan, J., Rajebhosale, P., Pittenger, S.T., Role, L.W., Talmage, D.A., et al. (2020). Acetylcholine is released in the basolateral amygdala in response to predictors of reward and enhances the learning of cue-reward contingency. Elife *9*, 573355–e57431. https://doi.org/10.7554/ELIFE.57335.
17. Zhu, F., Elnozahy, S., Lawlor, J., and Kuchibhotla, K.V. (2023). The cholinergic basal forebrain provides a parallel channel for state-dependent sensory signaling to auditory cortex. Nat. Neurosci. *26*, 810–819. https://doi.org/10.1038/s41593-023-01289-5.
18. Edeline, J.M., and Weinberger, N.M. (1992). Associative Retuning in the Thalamic Source of Input to the Amygdala and Auditory Cortex: Receptive Field Plasticity in the Medial Division of the Medial Geniculate Body. Behav. Neurosci. *106*, 81–105. https://doi.org/10.1037/0735-7044.106.1.81.
19. Taylor, J.A., Hasegawa, M., Benoit, C.M., Freire, J.A., Theodore, M., Ganea, D.A., Innocenti, S.M., Lu, T., and Gründemann, J. (2021). Single cell plasticity and population coding stability in auditory thalamus upon associative learning. Nat. Commun. *12*, 2438–2514. https://doi.org/10.1038/s41467-021-22421-8.
20. Belén Pardi, M., Vogenstahl, J., Dalmay, T., Spanò, T., Pu, D.L., Naumann, L.B., Kretschmer, F., Sprekeler, H., and Letzkus, J.J. (2020). A thalamocortical top-down circuit for associative memory. Science *370*, 844–848. https://doi.org/10.1126/SCIENCE.ABC2399/SUPPL_FILE/ABC2399_PARDI_SM.PDF.
21. Weinberger, N.M. (2004). Specific long-term memory traces in primary auditory cortex. Nat. Rev. Neurosci. *5*, 279–290. https://doi.org/10.1038/nrn1366.
22. Jiang, L., Kundu, S., Lederman, J.D.D., López-Hernández, G.Y.Y., Ballinger, E.C.C., Wang, S., Talmage, D.A.A., and Role, L.W.W. (2016). Cholinergic Signaling Controls Conditioned Fear Behaviors and Enhances Plasticity of Cortical-Amygdala Circuits. Neuron *90*, 1057–1070. https://doi.org/10.1016/J.NEURON.2016.04.028/ATTACHMENT/4D953C2D-B9B7-4572-BE15-A4AF11824B59/MMC2.MP4.
23. Likhtik, E., and Johansen, J.P. (2019). Neuromodulation in circuits of aversive emotional learning. Nat. Neurosci. *22*, 1586–1597. https://doi.org/10.1038/S41593-019-0503-3.
24. Aizenberg, M., Rolón-Martínez, S., Pham, T., Rao, W., Haas, J.S., and Geffen, M.N. (2019). Projection from the Amygdala to the Thalamic Reticular Nucleus Amplifies Cortical Sound Responses. Cell Rep. *28*, 605–615.e4. https://doi.org/10.1016/J.CELREP.2019.06.050/ATTACHMENT/2C5C4AC0-5CD3-487C-989F-06B5144C6B7C/MMC1.PDF.
25. Chavez, C., and Zaborszky, L. (2017). Basal forebrain cholinergic-auditory cortical network: primary versus nonprimary auditory cortical areas. Cerebr. Cortex *27*, 2335–2347. https://doi.org/10.1093/cercor/bhw091.
26. Tasaka, G. ichi, Feigin, L., Maor, I., Groysman, M., DeNardo, L.A., Schiavo, J.K., Froemke, R.C., Luo, L., and Mizrahi, A. (2020). The Temporal Association Cortex Plays a Key Role in Auditory-Driven Maternal Plasticity. Neuron *107*, 566–579. https://doi.org/10.1016/J.NEURON.2020.05.004/ATTACHMENT/31520E6A-D69C-402E-854C-F63AC03DFE85/MMC2.XLSX.
27. Tsukano, H., Hou, X., Horie, M., Kitaura, H., Nishio, N., Hishida, R., Takahashi, K., Kakita, A., Takebayashi, H., Sugiyama, S., and Shibuki, K. (2019). Reciprocal connectivity between secondary auditory cortical field and amygdala in mice. Sci. Rep. *9*, 19610–19612. https://doi.org/10.1038/s41598-019-56092-9.
28. Yang, Y., Liu, D.Q., Huang, W., Deng, J., Sun, Y., Zuo, Y., and Poo, M.M. (2016). Selective synaptic remodeling of amygdalocortical connections associated with fear memory. Nat. Neurosci., 1348–1355. https://doi.org/10.1038/nn.4370.
29. Letzkus, J.J., Wolff, S.B.E., Meyer, E.M.M., Tovote, P., Courtin, J., Herry, C., and Lüthi, A. (2011). A disinhibitory microcircuit for associative fear learning in the auditory cortex. Nature *480*, 331–335. https://doi.org/10.1038/NATURE10674.
30. Ceballo, S., Piwkowska, Z., Bourg, J., Daret, A., and Bathellier, B. (2019). Targeted Cortical Manipulation of Auditory Perception. Neuron *104*, 1168–1179. https://doi.org/10.1016/J.NEURON.2019.09.043/ATTACHMENT/B022ECF4-4880-48AC-8BC7-C5869E489E5F/MMC1.PDF.
31. Likhtik, E., Stujenske, J.M., Topiwala, M.A., Harris, A.Z., and Gordon, J.A. (2013). Prefrontal entrainment of amygdala activity signals safety in learned fear and innate anxiety. Nat. Neurosci. *17*, 106–113. https://doi.org/10.1038/nn.3582.

32. Taub, A.H., Perets, R., Kahana, E., and Paz, R. (2018). Oscillations Synchronize Amygdala-to-Prefrontal Primate Circuits during Aversive Learning. Neuron *97*, 291–298.e3. https://doi.org/10.1016/J.NEURON.2017.11.042.

33. Cambiaghi, M., Grosso, A., Likhtik, E., Mazziotti, R., Concina, G., Renna, A., Sacco, T., Gordon, J.A., and Sacchetti, B. (2016). Higher-Order Sensory Cortex Drives Basolateral Amygdala Activity during the Recall of Remote, but Not Recently Learned Fearful Memories. J. Neurosci. *36*, 1647–1659. https://doi.org/10.1523/JNEUROSCI.2351-15.2016.

34. Abs, E., Poorthuis, R.B., Apelblat, D., Muhammad, K., Pardi, M.B., Enke, L., Kushinsky, D., Pu, D.L., Eizinger, M.F., Conzelmann, K.K., et al. (2018). Learning-related plasticity in dendrite-targeting layer 1 interneurons. Neuron *100*, 684–699.e6. https://doi.org/10.1016/j.neuron.2018.09.001.

35. Gillet, S.N., Kato, H.K., Justen, M.A., Lai, M., and Isaacson, J.S. (2017). Fear learning regulates cortical sensory representations by suppressing habituation. Front. Neural Circ. *11*, 112. https://doi.org/10.3389/FNCIR.2017.00112/BIBTEX.

36. Schroeder, A., Pardi, M.B., Keijser, J., Dalmay, T., Groisman, A.I., Schuman, E.M., Sprekeler, H., and Letzkus, J.J. (2023). Inhibitory top-down projections from zona incerta mediate neocortical memory. Neuron *0*. https://doi.org/10.1016/J.NEURON.2022.12.010/ATTACHMENT/19A2A5A0-03AC-4CB8-9103-B5E6984D5A1E/MMC2.XLSX.

37. Weinberger, N.M., and Diamond, D.M. (1987). Physiological plasticity in auditory cortex: Rapid induction by learning. Prog. Neurobiol. *29*, 1–55. https://doi.org/10.1016/0301-0082(87)90014-1.

38. Gehrlach, D.A., Dolensek, N., Klein, A.S., Roy Chowdhury, R., Matthys, A., Junghänel, M., Gaitanos, T.N., Podgornik, A., Black, T.D., Reddy Vaka, N., et al. (2019). Aversive state processing in the posterior insular cortex. Nat. Neurosci. *22*, 1424–1437. https://doi.org/10.1038/S41593-019-0469-1.

39. Oleson, T.D., Westenberg, I.S., and Weinberger, N.M. (1972). Characteristics of the pupillary dilation response during pavlovian conditioning in paralyzed cats. Behav. Biol. *7*, 829–840. https://doi.org/10.1016/S0091-6773(72)80175-5.

40. Bimbard, C., Sit, T.P.H., Lebedeva, A., Reddy, C.B., Harris, K.D., and Carandini, M. (2023). Behavioral origin of sound-evoked activity in mouse visual cortex. Nat. Neurosci. *26*, 251–258. https://doi.org/10.1038/s41593-022-01227-x.

41. Meyer, A.F., Poort, J., O'Keefe, J., Sahani, M., and Linden, J.F. (2018). A Head-Mounted Camera System Integrates Detailed Behavioral Monitoring with Multichannel Electrophysiology in Freely Moving Mice. Neuron *100*, 46–60.e7. https://doi.org/10.1016/j.neuron.2018.09.020.

42. Stringer, C., Pachitariu, M., Steinmetz, N., Reddy, C.B., Carandini, M., and Harris, K.D. (2019). Spontaneous behaviors drive multidimensional, brainwide activity. Science *364*, 255. https://doi.org/10.1126/SCIENCE.AAV7893/SUPPL_FILE/AAV7893_STRINGER_SM.PDF.

43. Romero, S., Hight, A.E., Clayton, K.K., Resnik, J., Williamson, R.S., Hancock, K.E., and Polley, D.B. (2020). Cellular and widefield imaging of sound frequency organization in primary and higher order fields of the mouse auditory cortex. Cerebr. Cortex *30*, 1603–1622. https://doi.org/10.1093/cercor/bhz190.

44. Feigin, L., Tasaka, G., Maor, I., and Mizrahi, A. (2021). Sparse Coding in Temporal Association Cortex Improves Complex Sound Discriminability. J. Neurosci. *41*, 7048–7064. https://doi.org/10.1523/JNEUROSCI.3167-20.2021.

45. Stiebler, I., Neulist, R., Fichtel, I., and Ehret, G. (1997). The auditory cortex of the house mouse: Left-right differences, tonotopic organization and quantitative analysis of frequency representation. J. Comp. Physiol. *181*, 559–571. https://doi.org/10.1007/S003590050140/METRICS.

46. Narayanan, D.P., Tsukano, H., Kline, A.M., Onodera, K., and Kato, H.K. (2023). Biological constraints on stereotaxic targeting of functionally-defined cortical areas. Cerebr. Cortex *33*, 3293–3310. https://doi.org/10.1093/CERCOR/BHAC275.

47. Allsop, S.A., Wichmann, R., Mills, F., Burgos-Robles, A., Chang, C.J., Felix-Ortiz, A.C., Vienne, A., Beyeler, A., Izadmehr, E.M., Glober, G., et al. (2018). Corticoamygdala Transfer of Socially Derived Information Gates Observational Learning. Cell *173*, 1329–1342. https://doi.org/10.1016/J.CELL.2018.04.004/ATTACHMENT/45655FA1-E57D-408F-AA75-A61EE0F3620A/MMC2.MP4.

48. LeDoux, J.E. (2000). Emotion circuits in the brain. Annu. Rev. Neurosci. *23*, 155–184.

49. Letzkus, J.J., Wolff, S.B.E., and Lüthi, A. (2015). Disinhibition, a Circuit Mechanism for Associative Learning and Memory. Neuron *88*, 264–276. https://doi.org/10.1016/J.NEURON.2015.09.024.

50. Pape, H.C., and Pare, D. (2010). Plastic synaptic networks of the amygdala for the acquisition, expression, and extinction of conditioned fear. Physiol. Rev. *90*, 419–463. https://doi.org/10.1152/PHYSREV.00037.2009/ASSET/IMAGES/LARGE/Z9J0021025350009.JPEG.

51. Sah, P., Westbrook, R.F., and Lüthi, A. (2008). Fear Conditioning and Long-term Potentiation in the Amygdala. Ann. N. Y. Acad. Sci. *1129*, 88–95. https://doi.org/10.1196/annals.1417.020.

52. Williamson, R.S., and Polley, D.B. (2019). Parallel pathways for sound processing and functional connectivity among layer 5 and 6 auditory corticofugal neurons. Elife *8*, e42974. https://doi.org/10.7554/ELIFE.42974.

53. Clayton, K.K., Williamson, R.S., Hancock, K.E., Tasaka, G.I., Mizrahi, A., Hackett, T.A., and Polley, D.B. (2021). Auditory Corticothalamic Neurons Are Recruited by Motor Preparatory Inputs. Curr. Biol. *31*, 310–321.e5. https://doi.org/10.1016/J.CUB.2020.10.027.

54. Krabbe, S., Gründemann, J., and Lüthi, A. (2018). Amygdala Inhibitory Circuits Regulate Associative Fear Conditioning. Biol. Psychiatr. *83*, 800–809. https://doi.org/10.1016/J.BIOPSYCH.2017.10.006.

55. Xiong, Q., Znamenskiy, P., and Zador, A.M. (2015). Selective corticostriatal plasticity during acquisition of an auditory discrimination task. Nature *521*, 348–351. https://doi.org/10.1038/nature14225.

56. Einevoll, G.T., Kayser, C., Logothetis, N.K., and Panzeri, S. (2013). Modelling and analysis of local field potentials for studying the function of cortical circuits. Nat. Rev. Neurosci. *11*, 770–785. https://doi.org/10.1038/nrn3599.

57. Laszlovszky, T., Schlingloff, D., Hegedüs, P., Freund, T.F., Gulyás, A., Kepecs, A., and Hangya, B. (2020). Distinct synchronization, cortical coupling and behavioral function of two basal forebrain cholinergic neuron types. Nat. Neurosci. *23*, 992–1003. https://doi.org/10.1038/s41593-020-0648-0.

58. Ehinger, B.V., and Dimigen, O. (2019). Unfold: an integrated toolbox for overlap correction, non-linear modeling, and regression-based EEG analysis. PeerJ *7*, e7838. https://doi.org/10.7717/PEERJ.7838.

59. McDonald, A.J., and Jackson, T.R. (1987). Amygdaloid connections with posterior insular and temporal cortical areas in the rat. J. Comp. Neurol. *262*, 59–77. https://doi.org/10.1002/cne.902620106.

60. Jiménez-Capdeville, M.E., and Dykes, R.W. (1996). Changes in cortical acetylcholine release in the rat during day and night: differences between motor and sensory areas. Neuroscience *71*, 567–579. https://doi.org/10.1016/0306-4522(95)00439-4.

61. Steriade, M. (2004). Acetylcholine systems and rhythmic activities during the waking–sleep cycle. In Progress in Brain Research Acetylcholine in the Cerebral Cortex (Elsevier), pp. 179–196. https://doi.org/10.1016/S0079-6123(03)45013-9.

62. Yu, A.J., and Dayan, P. (2002). Acetylcholine in cortical inference. Neural Network. *15*, 719–730. https://doi.org/10.1016/S0893-6080(02)00058-8.

63. Disney, A.A., and Higley, M.J. (2020). Diverse Spatiotemporal Scales of Cholinergic Signaling in the Neocortex. J. Neurosci. *40*, 720–725. https://doi.org/10.1523/JNEUROSCI.1306-19.2019.

64. McGinley, M.J., Vinck, M., Reimer, J., Batista-Brito, R., Zagha, E., Cadwell, C.R., Tolias, A.S., Cardin, J.A., and McCormick, D.A. (2015). Waking State: Rapid Variations Modulate Neural and Behavioral Responses. Neuron *87*, 1143–1161. https://doi.org/10.1016/j.neuron.2015.09.012.

65. Sarter, M., and Lustig, C. (2020). Forebrain Cholinergic Signaling: Wired and Phasic, Not Tonic, and Causing Behavior. J. Neurosci. *40*, 712–719. https://doi.org/10.1523/JNEUROSCI.1305-19.2019.

66. Jing, M., Li, Y., Zeng, J., Huang, P., Skirzewski, M., Kljakic, O., Peng, W., Qian, T., Tan, K., Zou, J., et al. (2020). An optimized acetylcholine sensor for monitoring in vivo cholinergic activity. Nat. Methods *17*, 1139–1146. https://doi.org/10.1038/S41592-020-0953-2.

67. Aizenberg, M., and Geffen, M.N. (2013). Bidirectional effects of aversive learning on perceptual acuity are mediated by the sensory cortex. Nat. Neurosci. *16*, 994–996. https://doi.org/10.1038/NN.3443.

68. Wood, K.C., Angeloni, C.F., Oxman, K., Clopath, C., and Geffen, M.N. (2022). Neuronal activity in sensory cortex predicts the specificity of learning in mice. Nat. Commun. *13*, 1167–1215. https://doi.org/10.1038/s41467-022-28784-w.

69. Quirk, G.J., Armony, J.L., and LeDoux, J.E. (1997). Fear conditioning enhances different temporal components of tone-evoked spike trains in auditory cortex and lateral amygdala. Neuron *19*, 613–624. https://doi.org/10.1016/s0896-6273(00)80375-x.

70. Gründemann, J. (2021). Distributed coding in auditory thalamus and basolateral amygdala upon associative fear learning. Curr. Opin. Neurobiol. *67*, 183–189. https://doi.org/10.1016/J.CONB.2020.11.014.

71. Leppla, C.A., Keyes, L.R., Gordon Glober, ·, Gillian, ·, Batra, K., Jay, M., Feng, Y., Chen, H.S., Mills, F., Mills, F., et al. (2022). Thalamus sends information about arousal but not valence to the amygdala. Psychopharmacology *240*, 477–499. https://doi.org/10.1007/S00213-022-06284-5.

72. Concina, G., Renna, A., Milano, L., and Sacchetti, B. (2022). Prior fear learning enables the rapid assimilation of new fear memories directly into cortical networks. PLoS Biol. *20*, e3001789. https://doi.org/10.1371/JOURNAL.PBIO.3001789.

73. Grewe, B.F., Gründemann, J., Kitch, L.J., Lecoq, J.A., Parker, J.G., Marshall, J.D., Larkin, M.C., Jercog, P.E., Grenier, F., Li, J.Z., et al. (2017). Neural ensemble dynamics underlying a long-term associative memory. Nature *543*, 670–675.

74. Hintiryan, H., Bowman, I., Johnson, D.L., Korobkova, L., Zhu, M., Khanjani, N., Gou, L., Gao, L., Yamashita, S., Bienkowski, M.S., et al. (2021). Connectivity characterization of the mouse basolateral amygdalar complex. Nat. Commun. *12*, 2859–2925. https://doi.org/10.1038/s41467-021-22915-5.

75. LeDoux, J.E., Farb, C.R., and Romanski, L.M. (1991). Overlapping projections to the amygdala and striatum from auditory processing areas of the thalamus and cortex. Neurosci. Lett. *134*, 139–144. https://doi.org/10.1016/0304-3940(91)90526-Y.

76. Gao, E., and Suga, N. (1998). Experience-dependent corticofugal adjustment of midbrain frequency map in bat auditory system. Proc. Natl. Acad. Sci. USA *95*, 12663–12670. https://doi.org/10.1073/PNAS.95.21.12663/ASSET/49642401-6DAC-413B-9117-5CA554D8FCA3/ASSETS/GRAPHIC/PQ2183236005.JPEG.

77. Liu, B.H., Huberman, A.D., and Scanziani, M. (2016). Cortico-fugal output from visual cortex promotes plasticity of innate motor behaviour. Nature *538*, 383–387. https://doi.org/10.1038/nature19818.

78. Zingg, B., Chou, X.L., Zhang, Z.G., Mesik, L., Liang, F., Tao, H.W., and Zhang, L.I. (2017). AAV-Mediated Anterograde Transsynaptic Tagging: Mapping Corticocollicular Input-Defined Neural Pathways for Defense Behaviors. Neuron *93*, 33–47. https://doi.org/10.1016/j.neuron.2016.11.045.

79. Asokan, M.M., Williamson, R.S., Hancock, K.E., and Polley, D.B. (2018). Sensory overamplification in layer 5 auditory corticofugal projection neurons following cochlear nerve synaptic damage. Nat. Commun. *9*, 1–10. https://doi.org/10.1038/s41467-018-04852-y.

80. Pisano, F., Pisanello, M., Lee, S.J., Lee, J., Maglie, E., Balena, A., Sileo, L., Spagnolo, B., Bianco, M., Hyun, M., et al. (2019). Depth-resolved fiber photometry with a single tapered optical fiber implant. Nat. Methods *16*, 1185–1192. https://doi.org/10.1038/s41592-019-0581-x.

81. Pachitariu, M., Steinmetz, N., Kadir, S., Carandini, M., and Kenneth D, H. (2016). Kilosort: realtime spike-sorting for extracellular electrophysiology with hundreds of channels. Preprint at bioRxiv. 061481. https://doi.org/10.1101/061481.

82. Asokan, M.M., Williamson, R.S., Hancock, K.E., and Polley, D.B. (2021). Inverted central auditory hierarchies for encoding local intervals and global temporal patterns. Curr. Biol. *31*, 1762–1770.e4. https://doi.org/10.1016/J.CUB.2021.01.076.

83. Rajebhosale, P., Ananth, M., Crouse, R., Jiang, L., Hernández, G.L.-, Arty, C., Wang, S., Jone, A., Zhong, C., Desai, N.S., et al. (2021). Basal forebrain cholinergic neurons are part of the threat memory engram. Preprint at bioRxiv. https://doi.org/10.1101/2021.05.02.442364.

84. Nath, T., Mathis, A., Chen, A.C., Patel, A., Bethge, M., and Mathis, M.W. (2019). Using DeepLabCut for 3D markerless pose estimation across species and behaviors. Nat. Protoc. *14*, 2152–2176. https://doi.org/10.1038/S41596-019-0176-0.

85. Mathis, A., Mamidanna, P., Cury, K.M., Abe, T., Murthy, V.N., Mathis, M.W., and Bethge, M. (2018). DeepLabCut: markerless pose estimation of user-defined body parts with deep learning. Nat. Neurosci. *21*, 1281–1289. https://doi.org/10.1038/s41593-018-0209-y.

86. Stringer, C., Pachitariu, M., Steinmetz, N., Reddy, C.B., Carandini, M., and Harris, K.D. (2019). Spontaneous behaviors drive multidimensional, brainwide activity. Science *364*, 255. https://doi.org/10.1126/SCIENCE.AAV7893/SUPPL_FILE/AAV7893_STRINGER_SM.PDF.

87. Shamash, P., Carandini, M., Harris, K.D., and Steinmetz, N.A. (2018). A tool for analyzing electrode tracks from slice histology. Preprint at bioRxiv. https://doi.org/10.1101/447995.

STAR★METHODS

KEY RESOURCES TABLE

REAGENT or RESOURCE	SOURCE	IDENTIFIER
Bacterial and virus strains		
AAVrg-pgk-cre	Addgene	24593-AAVrg
AAV5-Ef1a-DIO-hChR2-EYFP	Addgene	35509-AAV5
AAV9-hSyn-ACh3.0	WZ Biosciences	YL001003-AV9-PUB
Chemicals, peptides, and recombinant proteins		
CTB-AF555	Thermo Fisher Scientific	Cat# C34776
DiI	Thermo Fisher Scientific	Cat# V22885
Flow-It ALC Flowable Composite	Pentron	Cat# N11B
C&B Metabond Quick Adhesive Cement System	Parkell	Cat#S380
Mounting Medium with DAPI	VectorLabs	Cat# H-1500
Deposited data		
Source data	This paper; Mendeley Data	https://doi.org/10.17632/m2s6dry5s5.1
Experimental models: Organisms/strains		
Mouse: C57BL/6J	The Jackson Laboratory	Cat# JAX:000664; RRID:IMSR_JAX:000664
Software and algorithms		
LabVIEW	National Instruments	https://www.ni.com/en-us/shop/labview.html
Synapse	Tucker-Davis Technologies	https://www.tdt.com/component/synapse-software/
MATLAB	MathWorks	https://www.mathworks.com/products/matlab.html
Kilosort	GitHub	https://github.com/MouseLand/Kilosort
DeepLabCut	GitHub	https://github.com/DeepLabCut/DeepLabCut
Fiji	Fiji	RRID: SCR_002285; https://imagej.net/Welcome
Original code for data analysis	GitHub	https://github.com/Meenakshi-Asokan/Asokan_et_al_2023_CellReports
Other		
PXI	National Instruments	PXI-4461
Free-field speaker	Parts Express	Cat# 275-010
Free-field microphone	PCB Electronics	Cat# 378C01
CMOS camera	Teledyne Dalsa	Cat# G3-GM11-M2020
Lens	Tamron	Cat# 032938
IR longpass filter	MidOpt	Cat# LP830-25.5
IR LEDs	Vishay Semiconductors	Cat# VSLY5850
Precision Animal Shocker	Coulbourn Instruments	H13-15
Silicon recording probes	Cambridge NeuroTech	H2, H3
Neurodigitizer and Preamplifier	Tucker-Davis Technologies	PZ5
Data processer and real-time controller	Tucker-Davis Technologies	RZ2
Data streamer	Tucker-Davis Technologies	RS4
Headstage components	Tucker-Davis Technologies	ZC64
Hydraulic probe drive	FHC	Cat# 50-12-1C
Diode laser (473 nm)	Omicron	LuxX_473-100

(*Continued on next page*)

Continued

REAGENT or RESOURCE	SOURCE	IDENTIFIER
Fluorescence mini-cube	Doric	FMC4
Femtowatt Photoreceiver	Newport	2151
Fiber photometry digital signal processor	Tucker-Davis Technologies	RZ5D
Epifluorescence microscope	Leica	DM5500B
Confocal laser scanning microscope	Leica	SP8

RESOURCE AVAILABILITY

Lead contact

Further information and requests should be directed to and will be fulfilled by the lead contact, Meenakshi Asokan (ma0716@princeton.edu).

Materials availability

This study did not generate new unique reagents.

Data and code availability

- Original data will be deposited to Mendeley Data: https://doi.org/10.17632/m2s6dry5s5.1 and made publicly available as of the date of publication.
- The analysis codes used in the study will be available at GitHub: https://github.com/Meenakshi-Asokan/Asokan_et_al_2023_CellReports and made publicly available as of the date of publication.
- Any additional information required to reanalyze the data reported in this paper is available from the lead contact upon reasonable request.

EXPERIMENTAL MODEL AND SUBJECT DETAILS

Animal subjects

We used adult male and female C57BL6 mice (Jackson Labs 000664) aged 9-10 weeks at the time of recording. Mice were housed individually after undergoing a major survival surgery. Mice were maintained in a 12/12 light/dark cycle with food and water available *ad libitum* and experiments were performed during their dark cycle. All procedures were approved by the Massachusetts Eye and Ear Infirmary Animal Care and Use Committee and followed the guidelines established by the National Institute of Health for the care and use of laboratory animals. Pupil- and facial motion-indexed behavioral measurements were performed in 27 mice, of which 3 were excluded for pupil dilation analysis because of pupil occlusion. Dual-site LA and HO-AC electrophysiological recordings were performed in 11 of these mice; Dual-site LA and HO-AC cholinergic sensor fiber recordings were performed in 8 of these mice, of which two were excluded from the analysis of LA ACh levels because of imprecise placement of the fiber implant over LA.

METHOD DETAILS

Surgical preparation

Mice were anesthetized with isoflurane in oxygen (5% induction, 2% maintenance) and placed in a stereotaxic frame (Kopf Model 1900). A homeothermic blanket system was used to maintain body temperature at 36.6° (FHC). Lidocaine hydrochloride was administered subcutaneously to numb the scalp. At the conclusion of the procedure and 24hr post-recovery, buprenorphine (0.05 mg/kg) and meloxicam (0.1 mg/kg) were administered, and the animal was transferred to a warmed recovery chamber.

Head plate attachment

The dorsal surface of the scalp was retracted, and the periosteum was removed. The exposed skull surface was prepped with etchant (C&B metabond) and 70% ethanol before affixing a titanium head plate (iMaterialise) to the skull with dental cement (C&B Metabond). Mice were given at least 48 hours to recover, after which they were acclimated to the head fixation apparatus before the electrophysiological recordings.

Injections and fiber implantation

For all adeno associated viral vector (AAV) and retrograde tracer injections, mice were prepped as described above. For LA injections, we first leveled the head by ensuring that the left and right z coordinates for the lateral skull were within +/- 0.03 mm and

the z coordinate of lambda was within +/- 0.05 mm of bregma. For injections into the higher order auditory cortex (HO-ACtx), a portion of the temporalis muscle was retracted to expose the skull the over the right squamosal suture as it passes just dorsal to the rhinal fissure. Burr holes were made in the skull with a 31-gauge needle. Pulled glass micropipettes (Wiretrol II, Drummond) were backfilled with virus solution and injected into the target brain areas at 1 nl/s using a precision injection system (Nanoject III, Drummond) with a 5 or 8s delay between each injected bolus. LA injection coordinates were 1.7 mm posterior from bregma (approximated intersection of skull sutures), 3.45 mm lateral of midline, 3.75 mm below the pial surface. HO-AC injection coordinates were 3.1 mm posterior to the bregma, lateral to the temporal ridge and medial to the squamosal suture, and 0.5 mm below the pial surface. At least 10 minutes passed following each injection before the pipette was withdrawn.

Expression of ChR2 in HO-AC CAmy neurons

We injected 150 nl of AAVrg-pgk-cre (1.7 x 10^{13} genome copies/mL, Addgene 24593) into the LA for retrograde expression of cre in the amygdala-projecting cells and 200 nl of AAV5-Ef1a-DIO-hChR2-EYFP into the HO-AC for cre-dependent hChR2 expression (Addgene 35509, diluted to 10% in sterile saline from 2.7 x 10^{13} genome copies/mL, to minimize any evidence of cellular toxicity). We allowed 3 weeks for the virus incubation before performing electrophysiology experiments.

Retrograde tracing experiments

We injected 300 nl of Cholera Toxin Subunit B, Alexa Fluor 555 conjugate (CTB-AF555, Thermo Fisher Scientific) into the LA following the procedure above. Mice were euthanized 7-9 days after injections.

Expression and measurement of the genetically encoded fluorescent ACh sensor

We injected 200 nl of AAV9-hSyn-ACh3.0 (diluted 2.5% in sterile saline from 3.6 x 10^{13} genome copies/mL, WZ Biosciences YL001003-AV9-PUB) into LA and 300 nl of AAV9-hSyn-ACh3.0 (diluted 10% in sterile saline from 3.6 x 10^{13} genome copies/mL, WZ Biosciences YL001003-AV9-PUB) into HO-AC. An optic fiber was implanted following each injection such that the distal tip of the fiber terminated 0.15 – 0.25mm above the injection depth. We implanted a flat fiber into LA (Doric, NA 0.37, 5mm length) and an angled fiber (Doric, NA 0.37, 2mm length, 45 deg angle) into HO-AC. Both fibers featured a 0.2mm core diameter and zirconia ferrule (outer diameter 1.25mm). Fibers were fixed into place and optically sealed by applying dental cement mixed with Black India Ink to the exposed skull and head plate. We allowed 3 weeks for the virus incubation before performing bulk fiber measurements.

Electrophysiology

Preparation for acute insertion of high-density probes in awake, head-fixed mice

A ground wire was implanted atop the left occipital cortex via a small burr hole during the preceding head plate attachment procedure described above. On the day of the Habituation session, mice were briefly anesthetized with isoflurane in oxygen (5% induction, 2% maintenance) and two small (~1 x 1-1.5 mm) craniotomies were made in the right hemisphere using a scalpel, each centered on the prior injection location. A circular well was constructed around each craniotomy with UV-cured cement (Flow-It ALC Flowable Composite) and filled with lubricating ointment (Paralube Vet Ointment) and the isoflurane was discontinued. Mice were placed in a body cradle and their head was immobilized by attaching the headplate to a head fixation post. Recordings were performed inside a dimly lit single-wall sound attenuating recording chamber (Acoustic Systems) after allowing at least 30 minutes to fully recover from anesthesia. At the conclusion of each recording session, the craniotomy was flushed with saline, ointment re-applied, and the recording well was sealed with a cap of UV-cured cement.

Extracellular recordings

LA recordings were performed with a two-shank 64-channel silicon probe (Cambridge Neurotech; H2 probe, 25 μm spacing between contacts within a shank, and 200μm spacing between shanks). HO-AC recordings were made with a single shank optrode (Cambridge Neurotech; H3 probe with 20μm spacing between contacts. The attached optic fiber featured a flat tip (200μm core, 0.66 NA), a 200μm horizontal offset to the shank, and 125μm vertical offset between the fiber tip and most superficial channel. Probes were positioned with a micromanipulator (Narishige) and inserted via a hydraulic microdrive (FHC). HO-AC recordings were made with an oblique insertion angle that spanned AuV and TeA. The LA recording probe was lowered ventrally with the two shanks oriented medio-laterally while optogenetically activating CAmy neurons (473nm diode laser, Omicron, LuxX) with brief laser pulses (1 ms duration, 10 Hz, 20 mW) to identify light-activated multiunit activity. The distal tip of the LA recording probe was typically 3.7-4mm below the pial surface but the fine position was adjusted such that CAmy-evoked multiunit responses were nearly absent in the most ventral channel. Once both probes were in place, we allowed the brain to settle for approximately 15 mins before recordings began.

Fiber photometry

LEDs of different wavelengths provided a basis for separating ACh-dependent fluorescence (465nm) from ACh-independent (405nm) fluorescence. LEDs were modulated at 210Hz (465nm) and 330Hz (405nm), respectively, and combined through an integrated fluorescence mini-cube (FMC4, Doric). The optical patch cable was connected to the fiber implant via a zirconia mating sleeve to produce a tip power of 0.1 - 0.2mW. Bulk fluorescent signals were acquired with a femtowatt photoreceiver (2151, Newport) and digital signal processor (Tucker-Davis Technologies RZ5D). The signal was demodulated by the lock-in amplifier implemented in the processor, sampled at 1017Hz and low-pass filtered with a corner frequency at 20Hz. The optical fibers were prebleached overnight by setting both LEDs to constant illumination at a low power (<50μW).

Discriminative threat conditioning

DTC was performed in three phases: Habituation, Conditioning and Recall. For electrophysiology recordings, each phase was performed in a single daily session separated by approximately 24 hours. For fiber recordings, the Habituation phase was two sessions, Conditioning was three sessions, and Recall was one session, each separated by approximately 24 hours. Parameters for DTC including CS and aversive reinforcement were based on recent publications.[9,20] All sessions presented trains of five frequency modulated (FM) sweeps presented at 1Hz (0.5s duration, 70 dB sound pressure level, 50ms raised cosine onset and offset gating applied at the FM endpoints). Each of the five FM sweeps for a given trial either increased or decreased in frequency (5-20kHz or 20-5kHz, respectively) at a rate of 4 octaves/sec. Daily sessions consisted of 30 alternating upward FM or downward FM trials with a 20-180s inter-trial interval selected from a decaying exponential distribution to produce a flat hazard function. On Conditioning sessions, for one FM sweep direction, the CS+, the 5th FM sweep coincided with the onset of a mildly aversive tail-shock (1 s, 0.4 mA AC, Coulbourn Precision Animal Shocker) via pediatric cuff electrodes positioned ~1 cm apart at the center of the tail. The assignment of the CS+ FM sweep direction was counterbalanced between animals. The cradle and surrounding test apparatus was cleaned with 70% ethanol before Habituation and Conditioning sessions, and 0.2% acetic acid before the Recall session.

Pseudo-conditioning was performed identically, except that the timing of the 15 tail shocks, 15 upward FM sweep trains, and 15 downward FM sweep train were each separated by the 20-180 s inter trial interval. Audio stimuli were generated with a 24-bit digital-to-analog converter (National Instruments model PXI-4461), and presented via a free-field speaker (Parts Express 275-010) placed approximately 10 cm from the left (contralateral) ear canal. Free-field stimuli were calibrated using a wide-band free-field microphone (PCB Electronics, 378C01).

Pupillometry and facial videography

Video recordings of the pupil and face were acquired at 30Hz with a CMOS camera (Teledyne Dalsa, model M2020) outfitted with a lens (Tamron 032938) and infrared longpass filter (Midopt lp830, 25.5nm cutoff). Recordings were using infrared LEDs (850 nm, Vishay Semiconductors, VSLY5850) where additional ambient light in the visible spectrum was adjusted to maintain an intermediate steady state pupil diameter.

Histology

Deeply anesthetized mice were perfused transcardially with 0.01 M phosphate-buffered saline (PBS; pH = 7.4) followed by 4% formaldehyde in 0.01 M PBS. Brains were removed and stored in 4% formaldehyde for 12 h before transferring to cryoprotectant (30% sucrose in 0.01 M PBS) for at least 48 hrs. Coronal sections were cut at 40 μm thickness on a cryostat and coverslipped using Vectashield Mounting Medium with DAPI (Vector Labs). Sections were imaged with a 10X/0.40 NA dry objective using an epifluorescence microscope (Leica DM5500B) or under a 40X /1.30 NA oil immersion objective using a confocal laser scanning microscope (Leica SP8).

QUANTIFICATIONS AND STATISTICAL ANALYSIS

Electrophysiology data acquisition

Raw neural signals were digitized at 32-bit, 24.4 kHz and stored in binary format (PZ5 Neurodigitizer, RZ2 BioAmp Processor, RS4 Data Streamer; Tucker-Davis Technologies). To eliminate artifacts, electrical signals were notch filtered at 60 Hz, and the Common-mode signal (channel-averaged trace) was subtracted from the raw signals from all channels, independently for each probe. For online visualization only, signals were band-pass filtered (300-3000 Hz, second-order Butterworth filters) and multiunit activity was extracted as negative deflections in the electrical trace with an amplitude exceeding 4 standard deviations of the baseline hash.

Single unit identification and analyses

Single unit isolation

We used Kilosort2[81] to sort spikes into single unit clusters. For recordings done on Habituation and Recall sessions, we concatenated all data files from a given session so that the same unit could be tracked over the full course of the single day experiment (~90 min). We ensured our units were isolated clusters with inter-spike intervals > 2ms for at least 95% of all spikes. Once isolated, spike waveforms with trough to peak intervals > 0.6ms were classified as regular spiking putative excitatory neurons, while intervals < 0.6ms were classified as fast spiking putative inhibitory interneurons, as per our previous work.[82]

Optogenetic identification of corticoamygdalar (CAmy) units

We operationally defined units with a high laser evoked spiking rate (> 5 standard deviations above prestimulus baseline), low first spike latency (< 5 ms) and a low first spike jitter (standard deviation of first spike latency < 0.75ms) in response to a 1ms 20mW laser pulse stimulation presented at 1Hz as the photo-identified CAmy units.

Analysis of evoked firing rate and stimulus synchrony

Only neurons that fired at least 0.01 Hz across the whole session were included for analysis. CS-evoked firing rates were measured in units with a peak firing rate >1.5 standard deviation above pre-stimulus baseline during the post-stimulus response period for the first FM sweep of the train for either CS, as determined with 1ms binning. The CS-evoked response used for computing the discriminative plasticity was quantified as the area under the curve of the peri-stimulus time histograms (PSTH) over the 5s CS duration. Asymmetry

indices were computed as $\frac{m_{CS+} - m_{CS-}}{m_{CS+} + m_{CS-}}$ where *m* is a measure with positive values such as neural firing rate (in spikes/s). Stimulus synchrony of the units was visualized using the firing rate averaged over 30 upward and downward sweeps and expressed as a z-score with respect to the baseline firing during a 1s duration before the sound onset. It was quantified as the amplitude at 1Hz of the fast Fourier transform of this z-scored firing rate during the 5s CS duration.

Neural population trajectories

Trial-averaged spike rates were expressed as z-scores relative to the distribution of pre-stimulus firing rates and smoothed with a 100ms gaussian filter. We then constructed a matrix with the concatenated responses to each CS for each unit on a row. The mean response for each unit was then subtracted from all column values. We performed singular value decomposition on this matrix using the Matlab function 'svd', and obtained its projections onto the transformed subspace, thereby reducing dimensionality using principal component analysis. To visualize the neural population trajectories, we plot the temporal evolution of the responses to each CS in the space defined by the first three principal components. To compute the Euclidian distance between the CS trajectories, we use the number of dimensions that are necessary to explain 80% of the variance in the data.

Local field potential extraction and analyses

LFP extraction

To extract the LFPs, raw signals from each channel of the recording electrodes were notch filtered at 60 Hz, down-sampled to 1000 Hz and spatially smoothed with a triangle filter (5-point Hanning window). We then subtracted the Common-mode reference (average signal across all channels) from each channel.

Analysis of evoked LFP amplitudes

CAmy-evoked LFP response in LA was measured by stimulating the CAmy cells using 100 repetitions of a 1ms 0-20 mW laser pulse presented at 4Hz. The CAmy-evoked LFP amplitude for each channel in LA was computed as the absolute value of peak of the deflection of the averaged LFP response in the 50ms duration following the laser pulse. The sound-evoked LFP amplitudes in each channel were expressed as the average instantaneous amplitude during the 5s CS duration calculated from the amplitude of the complex Hilbert transform of the LFP.

Spike-triggered LFPs

Network-level functional coupling was estimated from the spike-triggered LFP (stLFP). To estimate the stLFP, we used linear deconvolution by time expansion. The LFP measured in one region, for example LA (y) was interpreted as a sum of the linear convolution of the spiking events in the other region, for example HO-AC with the isolated (HO-AC → LA) stLFP (ß), and all the other possible sources (e) in:

$$y = X_{design} \cdot ß + e$$

Deconvolution was used to recover the unknown stLFP given only the measured LFP and the time of the spiking events (which is used to construct the design matrix), and estimate the stLFP that best explain the observed LFP given the spike times.[58] The spiking events can occur at any temporal interval between each other, and it is assumed that their contributions to y will linearly add up. We created a time-expanded version of the design matrix (X_{design}) with several time points around each event added as predictors and we then solved the model for the stLFP. The stLFP evoked by each unit was averaged across all channels in the other region. Since the sign of the stLFP deflection varies across depth along the probe after common-mode referencing, positive-deflecting traces were inverted before averaging.[57]

Photometry signal pre-processing and analyses

We calculated the ACh3.0 responses as the percentage fractional change in fluorescence $\Delta F/F_0$ (%), where F_0 was defined as the running median fluorescence value in a 60 s time window. To reduce the potential contribution of intrinsic signals and movement artifacts, analyses were performed on a corrected ACh3.0 signal in which the fractional change in fluorescence measured with the 405nm excitation was smoothed using a 1 s gaussian filter and then subtracted from the 465nm signal for each trial.[83] To capture learning-associated changes in ACh release while excluding time periods associated with tail shock and resultant changes in movement and arousal, we quantified CS-evoked responses during the initial 4s of the auditory cue period as the area under the curve of these corrected ACh3.0 signal during the initial 4s CS period (Figure 6F, dashed lines).

Pupil dilation response

Pupil diameter (P) was measured with DeepLabCut (version 2.0).[84,85] We labeled the four cardinal and four intercardinal points for the right pupil of each mouse in 10 frames each from 31 animals recorded under similar conditions. Training was performed on 95% of frames. We used a ResNet-101 based neural network with default parameters for 1.03 million training iterations. Each tracked point was expressed as a 3-D vector as x coordinate × y coordinate × time. Pupil diameter was estimated from the distance between East – West markers, which proved most robust to variations in eye lid position. Frames with the likelihood of these markers < 0.7 were discarded (e.g., during blink) and values were determined by interpolation. The sound-evoked pupil dilation was computed as a fractional change in pupil diameter ($\Delta P/P_0$) with respect to the mean pupil diameter at baseline (P_0, 2s before sound onset).

Facial motion response

As per previous work,[86] facial motion energy was measured at time T as the absolute value of the difference in pixel intensities between consecutive frames (T, T+1) for each pixel within the region of interest. We then positioned a region of interest (ROI) on the rostral cheek, just caudal to the vibrissae array, and defined facial motion (F) as a sum of the total motion energy for all pixels within the region of interest. We then expressed the sound-evoked facial motion for each trial as a fractional change ($\Delta F/F_0$) with respect to the mean facial motion in the baseline (F_0, 2s before sound onset).

Analysis of brain sections

Cell count quantification

To count CTB-labeled cells in the auditory cortex, we first used SHARP-Track[87] to register the photomicrographs with the Allen brain atlas. The center of each labeled cell was then marked with image processing software (Fiji) and the coordinates of each point was saved. We then marked the pial surface as a line and ran a function (developed by Michael Cammer, Microscopy core NYU Langone Medical Center) to compute the shortest distance of all the cells from the indicated pial surface.

Reconstruction of electrode tracks and fiber tips from photomicrographs

To validate the electrophysiology recording locations, probe shanks were dipped in a fluorescent lipophilic dye (DiI, Sigma-Aldrich 42364) before the final recording session and their insertion paths reconstructed from post-mortem photomicrographs using SHARP-Track.[87] Fiber tips were manually identified in the post-mortem sections after registering the slices to the Allen Brain Atlas.

Statistical analysis

All statistical analysis was performed with MATLAB (Mathworks). Non-parametric statistical tests were used in cases where data samples did not meet the assumptions of parametric statistical tests. Effect sizes were estimated with Cohen's d for normally distributed data and with Cliff's delta for samples that did not conform to a normal distribution. We used the standard p-value < 0.05 for assigning statistical significance denoted by asterisk symbol. The standard p-value was used in conjunction with a Cohen's $d > 0.4$ (or Cliff's delta > 0.3, which are traditionally assigned to a medium-sized effects or greater) in cases where the sample size was high (>25). Multiple post-hoc comparisons were corrected using Bonferroni-Holm correction.